



HAL
open science

Direct validation of dune instability theory

Ping Lü, Clément Narteau, Zhibao Dong, Philippe Claudin, Sébastien Rodriguez, Zhishan An, Laura Fernandez-Cascales, Cyril Gadat, Sylvain Courrech Du Pont

► **To cite this version:**

Ping Lü, Clément Narteau, Zhibao Dong, Philippe Claudin, Sébastien Rodriguez, et al.. Direct validation of dune instability theory. Proceedings of the National Academy of Sciences of the United States of America, 2021, 118 (17), pp.e2024105118. 10.1073/pnas.2024105118 . hal-03373712

HAL Id: hal-03373712

<https://hal.sorbonne-universite.fr/hal-03373712v1>

Submitted on 11 Oct 2021

HAL is a multi-disciplinary open access archive for the deposit and dissemination of scientific research documents, whether they are published or not. The documents may come from teaching and research institutions in France or abroad, or from public or private research centers.

L'archive ouverte pluridisciplinaire **HAL**, est destinée au dépôt et à la diffusion de documents scientifiques de niveau recherche, publiés ou non, émanant des établissements d'enseignement et de recherche français ou étrangers, des laboratoires publics ou privés.

Direct validation of dune instability theory

Ping Lü^{a,1,2}, Clément Narteau^{b,1,2}, Zhibao Dong^a, Philippe Claudin^c, Sébastien Rodriguez^b, Zhishan An^d, Laura Fernandez-Cascales^b, Cyril Gadal^b, and Sylvain Courrech du Pont^e

^aSchool of Geography and Tourism, Shaanxi Normal University, 620 Chang'an West Avenue, Xi'an, Shaanxi 710119, China; ^bUniversité de Paris, Institut de physique du Globe de Paris, CNRS, F-75005 Paris, France; ^cPhysique et Mécanique des Milieux Hétérogènes, CNRS, ESPCI, PSL Research Univ, Sorbonne Univ, Université de Paris, 10 rue Vauquelin, 75005 Paris, France; ^dNorthwest Institute of Eco-Environment and Resources, Donggang West Road 320, Lanzhou, Gansu Province 730000, China; ^eLaboratoire Matière et Système Complexes, Université de Paris, CNRS, 10 rue Alice Domon et Léonie Duquet, 75205 Paris Cedex 13, France

This manuscript was compiled on June 25, 2021

An edited version of this paper was published by PNAS under the PNAS licence: Lü, P., Narteau, C., Dong, Z., Claudin, P., Rodriguez, S., An, Z., Fernandez-Cascales, L., Gadal, C. and du Pont, S.C., 2021. Direct validation of dune instability theory. *Proceedings of the National Academy of Sciences*, 118(17), doi/10.1073/pnas.2024105118.

Modern dune fields are valuable sources of information for the large-scale analysis of terrestrial and planetary environments and atmospheres, but their study relies on understanding the small-scale dynamics that constantly generate new dunes and reshape older ones. Here we designed a landscape-scale experiment at the edge of the Gobi desert, China, to quantify the development of incipient dunes under the natural action of winds. High-resolution topographic data documenting 42 months of bedform dynamics are examined to provide a spectral analysis of dune pattern formation. We identified two successive phases in the process of dune growth, from the initial flat sand bed to a meter-high periodic pattern. We focus on the initial phase, when the linear regime of dune instability applies, and measure the growth rate of dunes of different wavelengths. We identify the existence of a maximum growth rate, which readily explains the mechanism by which dunes select their size, leading to the prevalence of a 15 m-wavelength pattern. We quantitatively compare our experimental results to the prediction of the dune instability theory using transport and flow parameters independently measured in the field. The remarkable agreement between theory and observations demonstrates that the linear regime of dune growth is permanently expressed on low-amplitude bed topography, before larger regular patterns and slip faces eventually emerge. Our experiment underpin existing theoretical models for the early development of eolian dunes, which can now be used to provide reliable insights into atmospheric and surface processes on Earth and other planetary bodies.

Dune instability | Size-selection | Sediment transport | Surface winds

Dune research has always been stimulated by the question of the origin of periodic bedforms that are ubiquitous in sand seas at all scales (1–3). Answering this question has proven challenging, largely because of the variety of initial and boundary conditions spanned by places where regular dune patterns are observed (4–6). In addition, considerable uncertainty exists on the efficiency of the mechanisms of dune size-selection due to a dearth of reliable experiments on eolian dune growth. Quantitative analysis of incipient dune formation is therefore a prerequisite for a better physical understanding not only of the evolution of dune systems but also of transport and flow properties responsible for the emergence of a characteristic length scale.

Underwater experiments have shown that, as soon as the flow is strong enough to transport grains, a flat sand bed destabilizes into periodic bedforms propagating at a constant speed (7–14). However, wind tunnel experiments and Ralph Bagnold's attempts in the field to create artificial dunes have failed because the initial sand piles were not large enough

(15, 16). There is indeed a minimum length-scale for the formation of dunes, which has been estimated to be of the order of 10 m in eolian systems on Earth based on the smallest wavelength of the superimposed bedforms observed on the flanks of large dunes (17–19). After 20 years of intensive research, this characteristic length-scale is assumed to be regulated by the balance between a destabilizing process associated with the turbulent flow response to the topography and a stabilizing process due to transport inertia (20).

Fluid mechanics studies have shown that the flow above low dunes can be decomposed into an inner and an outer layer (21). In the outer layer, the flow perturbation is in phase with topography (i.e., wind speed is maximum above the dune crest). In the inner layer (the thin region adjacent to the bed), the effect of friction causes the wind velocity to be phase-advanced (22, 23). The theory predicts that this layer has a thickness, l , that shows a positive dependence on the wavelength, λ , of the bedforms. Within this layer, the maximum (minimum) wind speed is upwind of the maximum (minimum) of topography. For a sinusoidal topography, this perturbation takes the form of a phase shift, φ_b , which is usually described with two terms, $\cos(kx + \varphi_b) = A \cos(kx) + B \cos(kx + \pi/2)$, where $k = 2\pi/\lambda$ is the dune wave number. The in-phase term has a weight

Significance Statement

We report a landscape-scale experiment with controlled initial and boundary conditions to reveal incipient dune growth under the natural action of wind. We measured the growth rate of dunes of different wavelengths for 42 months in a desert plot of 7,500 m². We identify an early phase in which a clear maximum growth rate occurs for a 15 m dune spacing. A successful comparison with dune instability theory allows to quantify the size-selection mechanism leading to the emergence of periodic dune patterns, which can be directly related to flow and sand transport properties. An experiment of this type and scale is unprecedented. Its results boost confidence in the existing theory, confirming its application to a variety of planetary landscapes from repeated aerial/orbital imagery.

P.L. and C.N. carried out all statistical data analysis, helped by C.G. for dispersion relations. P.L., C.N., P.C. and S.C.P. designed the experimental study. P.L. and Z.D. managed the experimental site and P.L. led the acquisition of data in the field. Z.A. performed all laser scans. S.R. and L.F.C. acquired and analyzed wind profiles. C.N., P.C., S.R. and S.C.P. wrote the manuscript. All authors participate to field work and discussed the results.

There is no competing interest.

¹P.L. contributed equally to this work with C.N.

²To whom correspondence should be addressed. E-mail: lvping@snnu.edu.cn, narteau@ipgg.fr

coefficient A . The other, in phase quadrature, has a weight coefficient B . Then, the upwind shift between the wind speed and the bed topography can be expressed as $\arctan(B/A)/k$. Since the dune crest is a zone of decreasing wind speed, and therefore of sand deposition, this spatial shift is the essential ingredient for the initial growth of dunes (24). Nevertheless, the length scale associated with this spatial shift does not alone promote the dominance of any specific wavelength. Wavelength selection requires another antagonistic process, which relies on sand transport properties.

As sand flux adjusts to the aforementioned spatial change in wind speed, there is a spatial lag between the loci of maximum wind speed and maximum transport rate (25–27). This length scale is known as the saturation length l_{sat} , the distance required for the sand flux to reach saturation. The combined effect of this downwind shift in sand transport and the upwind shift in wind speed eventually acts as a size-selection mechanism. The minimum length scale for the formation of dunes arises at a characteristic wave number, k_0 , defined as the wave number for which these downwind and upwind shifts cancel each other out. At longer wavelengths ($k < k_0$), the crest is a zone of net deposition such that the dune grows. However, larger bedforms have longer response times which means that the growth rate also tends to zero in the limit $k \rightarrow 0$. There is therefore a characteristic wave number, k_{max} , for which the growth rate is maximum. It determines the most unstable wavelength, λ_{max} , and the characteristic length-scale for the emergence of periodic dunes.

Linear stability analysis of flat sand beds sheared by a fluid flow provide the analytical expression for the growth rates $\sigma(k)$ of sinusoidal bed perturbations over the whole range of possible wavelengths (6–8, 14, 16, 28–34). These stability analyses are by definition restricted to the linear regime of incipient dune growth, the period during which the amplitude of each mode (wavelength) grows exponentially and independently from one another. In this linear regime, a dispersion relation gives the growth rate of each mode as a function of the wave number. According to the flow and transport processes described above, theoretical dispersion relation can be expressed as

$$\sigma(k) = Q k^2 \frac{B - A k l_{\text{sat}}}{1 + (k l_{\text{sat}})^2}, \quad [1]$$

where Q is the mean sand flux, which can be derived from wind data and the threshold shear velocity, u_{th} , for the transport of sand grains (20). The numerator not only governs the initial dune growth (i.e., $\sigma(k) > 0$ for $k < k_0$ and $\sigma(k) < 0$ for $k > k_0$, where $k_0 = B/(A l_{\text{sat}})$) but also provides the essential mechanism for dune-size selection during the linear regime. Later, as dune aspect ratios become larger, dune dynamics enter a non-linear growth regime dominated by collisions and interactions between dunes of different sizes (35–39), and this dispersion relation no longer applies.

Focusing only on well-established periodic dune patterns, the existence of a characteristic wavelength for dune formation has been validated in various eolian environments using tools of comparative planetology (29) and in different places on Earth using superimposed bedforms (17) as well as incipient dunes in ephemeral channels (40) or at the border of dune fields (5). However, the dependence of the growth rate on dune size and the underlying size-selection mechanism associated with the emergence of periodic dunes have never been observed and

quantified in a natural eolian environment, nor in wind tunnels. To bridge this gap, we performed a long-term field experiment to measure, in the same desertic area, all of the parameters involved in the physics of dune growth. We present here a comprehensive description of incipient dune growth under the natural action of wind, which is directly confronted to the dune instability theory.

A landscape-scale experiment

In our landscape-scale experiments, we investigated dune dynamics at a scale of hundred of meters using controlled initial conditions and continuous monitoring of environmental conditions (41). These experiments started in 2009 in the Tengger Desert at the southeastern edge of the Gobi basin in China (Fig. 1A). This area is exposed to a bidirectional wind regime (Fig. 1B). The primary wind blows from the northwest mainly in the spring when the Siberian high-pressure system weakens. In summer, the easterly wind of the east-Asian monsoon dominates. Since November 2013, wind data from a local airport located 10 km east of the field site are synchronized with the wind data from the local meteorological tower and a 2 m high wind tower located on the side of our new experimental plot (Fig. S1).

The experiments dedicated to incipient dune growth have been conducted from April 2014 to November 2017. Pre-existing dunes were leveled on April 9, 2014, to form a flat rectangular bed 100 m long and 75 m wide (Fig. 1C). The long axis of this rectangular area is aligned with the direction of the primary wind. We monitored dune growth over the following 42 months (Fig. 1D and E) through a series of 20 topographic surveys using a ground-based laser scanner. To get a better resolution on the early stage of dune growth and to account for windy periods, these topographic data are not regularly distributed in time and are more frequent in 2014 as well as in the spring and fall of each year. To compare datasets from different scans, we installed a reference system of concrete posts over the entire experimental dune field (Fig. S9). During each topographic survey, we scanned the experimental plot from four different locations. Depending on the local slopes, the density of points varied from 472 to 2368 points/m² with a centimetric height accuracy throughout the duration of the experiment.

Results

Sand transport properties. To measure the threshold wind speed for sand movement and estimate the local sand flux from wind data, we characterized sand transport in the field in a dedicated set of short-term experiments. As in most of the Tengger Desert, the mean grain size in the experimental area is of about 190 μm (Fig. S2). Using an impact sensor placed above a flat sand bed, we monitored saltation activity under winds of varying strength (42). As shown in Fig. 2, the empirical relation between wind speed and the impact rate yields an estimated threshold wind speed for aerodynamic entrainment of sand grains, $u_{\text{th}} = 0.23 \pm 0.04 \text{ m s}^{-1}$. Combining this threshold value with local wind data, we calculate the saturated sand flux on a flat sand bed using the eolian transport law of Ungar and Haff (13, 43, 44). From January 2014 to November 2017, the mean flux is $Q = 18.4 \pm 4.2 \text{ m}^2 \text{ yr}^{-1}$ (Tab. S1).

To estimate the saturation length, l_{sat} , we constructed a flat bed armored with coarse gravels and cobbles, which acted as a sand trap. At a time without active transport, we build a 12 m long, 3 m wide and 20 cm high flat sand berm immediately downwind of the coarse bed, as determined from the direction of the prevailing wind (Fig. 3A). We measure the surface elevation of this sand berm using the terrestrial laser scanner before and after a wind event (Fig. 3 B and C). The difference in topography along the wind direction gives the mean transport rate profile for this time interval (Figs. S3 and S4). Fig. 3D shows a net erosion on the whole sand slab, with an amplitude that dampens with respect to the downwind distance from the non-erodible bed. These observations indicate an increasing sand flux converging toward its saturated value. Assuming an exponential relaxation of the sand flux (27), we obtain $l_{\text{sat}} = 0.95 \pm 0.2$ m.

Flow perturbation over low sinusoidal bedforms. To estimate the values of the aerodynamic parameters A and B used in Eq. 1, we measured the flow properties in October 2013 on dunes of small amplitude in the neighborhood of the experimental site. After flattening, the same measurements for the estimation of the phase shift between wind speed and topography were repeated in November 2014 as well as in April and November 2015 over the incipient bedforms of our experimental plot. We recorded wind speed at heights of 4, 12, 50, and 100 cm above the bed by moving an anemometer mast upwind of a known elevation dune profile, which include in most cases a succession of crests and troughs (Figs. 4A and S5). The density of the measurements is higher near the crests and troughs in order to determine more precisely the position of the maximum and minimum wind speeds. Each measurement lasted at least 10 min with a sampling rate of 1 Hz. The wind speeds measured at different heights were synchronized and normalized by the wind speed measured at one meter high by a reference cup anemometer located at the top of a larger dune in the vicinity, which allowed us to reconstruct the perturbation in wind speed on low dunes at different stages of dune growth.

As predicted in the limit of low sinusoidal bedforms, Fig. 4B shows that the wind perturbation at all heights reflect the topography of the underlying incipient dunes, both in amplitude and wavelength. The amplitude of perturbation in wind speed decreases with height above the bed. More importantly, there is always an upwind shift in wind speed for the two bottom anemometers at heights of 4 and 12 cm, but not for the two top anemometers at heights of 50 and 100 cm. This indicates that, on incipient dunes in our experimental area, the thickness l of the inner-layer is between 12 and 50 cm. Within this inner layer, using the upwind shift (≈ 1 m) and the amplitude of the perturbation in wind speed recorded by the two bottom anemometers, we get $A = 3 \pm 1$ and $B = 1.5 \pm 0.5$ for dune aspect ratios varying from 0.012 to 0.025 (Fig. 4C and Tab. S2).

Emergence of a periodic dune pattern. Within the experimental plot, to avoid disturbances from the surrounding bedforms, we select a central rectangular area with a width of 48 m and a length of 82 m (red square in Fig. 1A). The long side of this rectangle is oriented Northwest-Southeast to align with the prevailing transport direction. We remove the mean slope of this rectangular area by fitting a plane to the elevation data.

Throughout the experiment, this plane maintained a gentle southwest-facing slope as observed after the flattening of the dune field. The residual topography is shown for different times in Fig. 5A. Within the observation area, we chose to follow the time evolution of elevation along 34 parallel transects with a constant spacing of 1.4 m. These transects are oriented perpendicularly to the final dune orientation observed in November 2017. Fig. 5B shows the elevation profiles with respect to time for a given transect. Over the 42 months of the experiment, the amplitude of the dunes increases by two orders of magnitude from a few centimeters to a few meters. Whereas no periodic pattern is discernible after flattening, a characteristic wavelength of 15 m emerges over the first few months of the experiment (Figs. 1D and 1E).

The variation of the mean amplitude of the dune pattern, defined as the root-mean-square of the topography, is not homogeneous over time and displays a sudden change in rate at the end of 2014 (Fig. 5C). Before, from April to October 2014, this amplitude stays almost constant. During this time period, despite a smoother topography, there is nothing to suggest that dunes will appear at a specific wavelength. Starting in November 2014, the surface elevation exhibits a periodic dune pattern with marked crestlines and a northeast-southwest orientation. Then, the mean amplitude increases significantly at a constant rate of 0.5 m yr^{-1} for three years (Fig. 5C). We found that the transition between these two different stages of dune growth occurs for a mean slope of the order of 0.03 (Fig. S6), when dune crests and slip faces emerge and begin to spatially organize throughout the experimental plot (Fig. S7). Steeper slopes highlights the increase in dune aspect ratio (6, 45), which is the main control parameter for aerodynamic non-linearities. Hence, we ascribe the two different stages to the linear and the non-linear phases of the dune growth instability.

Experimental dispersion relation for incipient dune growth.

Elevation profiles were repeatedly acquired at 20 different times at each of our 34 transect locations. We performed a spectral decomposition of these elevation profiles to isolate the contribution of individual modes (i.e., wavelengths) to the overall topography. Fig. 6A shows the amplitude of three different modes as a function of a dimensionless transport time scale, which is set to zero after flattening and is then incremented over time proportionally to sand flux (Fig. S8). Once again, abrupt changes in growth rate are observed in November 2014. Before, the amplitude of the different modes is found to vary exponentially with time, which is consistent with the linear regime of the dune instability.

For length scales ranging from 5 to 60 m, we measure the exponential growth rate of each mode from April to October 2014 using the dimensionless time (Figs. S9-S11). It is positive for large wavelengths, negative for small wavelengths, and reaches a maximum value for an intermediate wavelength of approximately 15 m. Plotting the growth rate of the different modes as a function of their wave number k , we obtain the experimental dispersion relation of the dune instability (Fig. 6B). The consistent variation of these growth rates over the entire range of length scales, the presence of clear maximum and the continuous trend from unstable (i.e., growing waves, $\sigma > 0$) to stable regimes (i.e., decaying waves, $\sigma < 0$) reflect most of the behaviors usually predicted during the linear phase of dune growth. Most importantly, it provides the first eolian experi-

mental evidence of the difference in growth rates of nascent dunes of various wavelengths when they are not large enough to generate flow recirculations.

Finally, we test the consistency of the theoretical prediction of the linear stability analysis by comparing the dispersion relations given by Eq. 1 to the experimental dispersion relation derived only from topographic data in the field. We either use fitted values for the parameters A , B , and l_{sat} , or we set them to the values we have independently measured in the field (Figs. 2-4). In both cases, we find a good quantitative agreement between the experimental and the theoretical dispersion relations (Figs. 6B and S12-S13). As shown by the shaded area in Fig. 4C and a B/A ratio close to 0.5 in both cases, the difference lies mainly in the sensitivity of the dispersion relation to the l_{sat} value.

Discussion

In order to meet the challenge of comparing and evaluating theoretical models of dune growth with observational data, the landscape-scale experiment conducted in an active dune field under the natural action of wind yield a unique set of new quantitative relationships. By removing uncertainties about boundary and initial conditions, we verify that dunes can emerge from a flat sand bed (46, 47) and validate the theory behind this dune growth mechanism. We elucidate the origin of periodic bedforms, showing the wavelength selection as dunes increase in height. Meanwhile, we highlight the inherent benefits of combining field observations with theory to derive information about the sediment transport and flow properties from the morphodynamics of incipient dunes.

Through experimental evidence in the field, this direct validation of dune instability theory transforms a working hypothesis into a comprehensive and operational model for the origin and initial growth of dune patterns. From a dispersion relation based on measurable physical quantities, such a model reveals the consistency of the size-selection mechanisms leading to the development of spatial structures in dune fields. As soon as a granular bed sheared by a flow leads to such an instability and the emergence of periodic dunes, their regular spacing corresponds to the most unstable mode, determining the balance between the downwind shift in sand transport (i.e., the saturation length) and the upwind shift in wind speed. The neutral mode ($\sigma(k_0) = 0$) sets the minimum length scale for the formation of dunes ($2\pi/k_0 \approx 9$ m in this area of the Tengger Desert), and is directly estimated from observations and the experimental dispersion relation.

We provide an original dataset for an in-depth understanding of the linear phase of the dune instability, when the growth rates of the different modes evolve independently from each other. We find that this linear phase is at work from the earliest stage of dune growth, as soon as sand transport starts even when, at first glance, no regular structure seems to be in place. It takes time for the most unstable wavelength to prevail over all the other modes that contribute to the sand bed topography. When periodic dunes are observed, the non-linear phase has already taken over, aerodynamic non-linearities have developed and the different modes interact with each other to lead to pattern coarsening (37, 38). We show here that the continuous transition from the linear to the non-linear regimes is controlled by the dune aspect-ratio for remarkably low values (≈ 0.03), consistent with laboratory measurements

on sinusoidal beds (20). This transition coincides with the spatial organisation of bedforms according to the alignment of mature dunes. For mean slope values of 0.07 (4° , typical of the flattest dune slopes), the transition is completed and it is no longer possible to differentiate between the growth rates of the different modes. Nevertheless, the most unstable mode can still be observed to provide relevant length and time scales of the dune instability.

Another objective of our series of measurements was to estimate changes in the upwind velocity shift at different stages of dune growth. A decreasing value of this phase shift would reduce the deposition rate at the crest and could naturally be associated with the selection of the steady aspect-ratio of dunes. This phenomenon can be expressed through a decrease in the values of the parameters A and B during the transition from the linear to the non-linear regime and the development of aerodynamic non-linearities. Thus, in addition to their weak (logarithmic) positive dependences on kz_s , where z_s is the aerodynamic roughness, a weakly non-linear expansion of the flow predicts that the parameters A and B have also a quadratic negative dependence on dune aspect-ratio (48). However, with our measurement precision and the range of measured dune aspect-ratio, we could not observe any systematic dependence of the value of the parameters A and B on dune growth, which remains a challenge that goes beyond the mechanism of size selection.

Landscape-scale experiments at the scale of thousands of m^2 and over many years are still extremely rare in the field of geomorphology and surface processes. Thanks to a series of high-resolution elevation maps, this study emphasizes that we can now achieve the precision needed to analyze the linear phase of eolian dune growth, a short but fundamental period during which regular dune patterns may still be imperceptible. More generally, our experiments bridge the gap between theoretical physics and geophysical surveys and can translate into concrete new research avenues across scientific domains. Instability theory applies to many natural systems, especially to examine the relationships between flow and surface properties on solid bedforms, icy or rocky, controlled by chemical reactions or phase changes (51, 52). For all these natural systems, we show here that, when the technological step in data acquisition is taken (49, 50), field studies can be carried out to test theoretical outputs against observations and to develop better forecasts of landscape morphogenesis.

The dispersion relation gives the range of wavelengths over which nascent dunes are likely to be observed. Then, in addition to the most unstable mode, we can now evaluate how other modes with lower growth rates contribute to the distribution of dune sizes encountered in dune fields. As it was done before using only the emerging dune pattern (6, 17, 40, 41), the evolution of bedforms over a wide range of length scales gives a more complete framework to derive information about the nature of the sediment and the atmospheric wind regimes from the morphodynamics of incipient dunes. This includes air and sediment densities, grain size, and the mean wind strength, which together determine the threshold wind speed for eolian transport.

Based on our comprehensive assessment of the dune instability, we showed here that successive topographic surveys and spectral analysis can be combined to characterize different environments on Earth and other planetary bodies where dunes

actively participate in landscape dynamics (29, 33, 50, 53–57). We provide quantitative evidence that such an inverse problem can be solved over relatively short time scales relative to those involved in the dynamics of major dune systems. This approach can be used to remotely assess sediment and atmospheric quantities. It is particularly relevant on planetary and cometary surfaces where bedforms can grow under exotic conditions with unusual parameter values (3, 58). The dune instability also occur on larger structures, and this is especially visible when the wind suddenly changes direction. An accurate, high-frequency topographic analysis based on the instability theory could then be performed at a local scale to document wind speed and direction as well as the duration of wind events.

Materials and Methods

The Supplementary Information includes wind data (Fig. S1), the grain size distribution (Fig. S2) as well as the equations and parameter values used to compute sand transport (Tab. S1). It also provides a detailed description of the field experiments and the equations used to estimate the saturation length, l_{sat} (Figs. S3 and S4) and the aerodynamic parameters A and B (Fig. S5 and Tab. S2). Then, it describes the solution strategy employed to obtain the dispersion relation from the topographic data (Figs. S6–S13).

ACKNOWLEDGMENTS. We acknowledge financial support from the National Natural Science Foundation of China (41871011 and 41930641), the UnivEarthS LabEx program (ANR-10-LABX-0023), the IdEx Université de Paris (ANR-18-IDEX-0001), the French National Research Agency (ANR-12-BS05-001-03/EXO-DUNES, ANR-17-CE01-0014/SONO), the National Science Center of Poland (grant 2016/23/B/ST10/01700), and the French Chinese International laboratory SALADYN.

1. E McKee, *A study of global sand seas*. (U.S. Geological Survey) Vol. Professional Paper 1052, (1979).
2. K Pye, H Tsoar, *Aeolian sand and sand dunes*. (Unwin Hyman, London), p. 458 (1990).
3. RD Lorenz, JR Zimbelman, *Dune worlds: How windblown sand shapes planetary landscapes*. (Springer Science & Business Media), (2014).
4. RC Ewing, GA Kocurek, Aeolian dune interactions and dune-field pattern formation: White Sands Dune Field, New Mexico. *Sedimentology* **57**, 1199–1219 (2010).
5. C Gadal, C Narteau, S Courrech du Pont, O Rozier, P Claudin, Periodicity in fields of elongating dunes. *Geology* **48**, 343–347 (2020).
6. C Gadal, et al., Spatial and temporal development of incipient dunes. *Geophys. Res. Lett.* **47**, e2020GL088919 (2020).
7. J Kennedy, The mechanics of dunes and antidunes in erodible bed channels. *J. Fluid Mech.* **16**, 521–544 (1963).
8. KJ Richards, The formation of ripples and dunes on an erodible bed. *J. Fluid Mech.* **99**, 597–618 (1980).
9. S Coleman, B Melville, Bed-form development. *J. Hydraul. Eng.* **120**, 544–560 (1994).
10. JH Baas, A flume study on the development and equilibrium morphology of current ripples in very fine sand. *Sedimentology* **41**, 185–209 (1994).
11. A Valance, V Langlois, Ripple formation over a sand bed submitted to a laminar shear flow. *The Eur. Phys. J. B-Condensed Matter Complex Syst.* **43**, 283–294 (2005).
12. E Reffet, S Courrech du Pont, P Hersen, S Douady, Formation and stability of transverse and longitudinal sand dunes. *Geology* **38**, 491–494 (2010).
13. S Courrech du Pont, C Narteau, X Gao, Two modes for dune orientation. *Geology* **42**, 743–746 (2014).
14. C Gadal, C Narteau, SC du Pont, O Rozier, P Claudin, Incipient bedforms in a bidirectional wind regime. *J. Fluid Mech.* **862**, 490–516 (2019).
15. RA Bagnold, *The physics of wind blown sand and desert dunes*. (Methuen, London) Vol. 265, (1941).
16. B Andreotti, P Claudin, S Douady, Selection of dune shapes and velocities part 1: Dynamics of sand, wind and barchans. *The Eur. Phys. J. B-Condensed Matter Complex Syst.* **28**, 321–339 (2002).
17. H Elbelrhiti, P Claudin, B Andreotti, Field evidence for surface-wave-induced instability of sand dunes. *Nature* **437**, 720–723 (2005).
18. EJ Parteli, O Duran, HJ Herrmann, Minimal size of a barchan dune. *Phys. Rev. E* **75**, 011301 (2007).
19. C Narteau, D Zhang, O Rozier, P Claudin, Setting the length and time scales of a cellular automaton dune model from the analysis of superimposed bed forms. *JGR: Earth Surf.* **114** (2009).
20. F Charru, B Andreotti, P Claudin, Sand ripples and dunes. *Annu. Rev. Fluid Mech.* **45**, 469–493 (2013).
21. PS Jackson, JCR Hunt, Turbulent wind flow over a low hill. *Q. J. Roy. Meteorol. Soc.* **101**, 929–955 (1975).
22. J Hunt, K Richards, P Brighton, Stably stratified shear flow over low hills. *Q. J. Royal Meteorol. Soc.* **114**, 859–886 (1988).
23. P Claudin, G Wiggs, B Andreotti, Field evidence for the upwind velocity shift at the crest of low dunes. *Boundary-layer Meteorol.* **148**, 195–206 (2013).
24. K Kroy, G Saueremann, HJ Herrmann, Minimal model for sand dunes. *Phys. Rev. Lett.* **88**, 054301 (2002).
25. G Saueremann, K Kroy, HJ Herrmann, Continuum saltation model for sand dunes. *Phys. Rev. E* **6403**, art. no.–031305 (2001).
26. T Pähz, JF Kok, EJ Parteli, HJ Herrmann, Flux saturation length of sediment transport. *Phys. Rev. Lett.* **111**, 218002 (2013).
27. B Andreotti, P Claudin, O Pouliquen, Measurements of the aeolian sand transport saturation length. *Geomorphology* **123**, 343–348 (2010).
28. B Andreotti, P Claudin, O Devauchelle, O Durán, A Fourrière, Bedforms in a turbulent stream: ripples, chevrons and antidunes. *J. Fluid Mech.* **690**, 94–128 (2012).
29. P Claudin, B Andreotti, A scaling law for aeolian dunes on Mars, Venus, Earth, and for sub-aqueous ripples. *Earth Planet. Sci. Lett.* **252**, 30–44 (2006).
30. M Colombini, Revisiting the linear theory of sand dune formation. *J. Fluid Mech.* **502**, 1–16 (2004).
31. O Devauchelle, et al., Stability of bedforms in laminar flows with free surface: from bars to ripples. *J. Fluid Mech.* **642**, 329–348 (2010).
32. PY Lagrée, A triple deck model of ripple formation and evolution. *Phys. Fluids* **15**, 2355–2368 (2003).
33. O Durán Vinent, B Andreotti, P Claudin, C Winter, A unified model of ripples and dunes in water and planetary environments. *Nat. Geosci.* **12**, 345–350 (2019).
34. A Fourrière, P Claudin, B Andreotti, Bedforms in a turbulent stream: formation of ripples by primary linear instability and of dunes by nonlinear pattern coarsening. *J. Fluid Mech.* **649**, 287–328 (2010).
35. RC Ewing, G Kocurek, LW Lake, Pattern analysis of dune-field parameters. *Earth Surf. Process. Landforms: The J. Br. Geomorphol. Res. Group* **31**, 1176–1191 (2006).
36. E Parteli, V Schwämmle, HJ Herrmann, L Monteiro, L Maia, Profile measurement and simulation of a transverse dune field in the lençóis maranhenses. *Geomorphology* **81**, 29–42 (2006).
37. A Valance, Nonlinear sand bedform dynamics in a viscous flow. *Phys. Rev. E* **83**, 036304 (2011).
38. X Gao, C Narteau, O Rozier, Development and steady states of transverse dunes: A numerical analysis of dune pattern coarsening and giant dunes. *J. Geophys. Res.* **120**, 2200–2219 (2015).
39. M Day, G Kocurek, Pattern similarity across planetary dune fields. *Geology* **46**, 999–1002 (2018).
40. P Delorme, et al., Dune initiation in a bimodal wind regime. *JGR: Earth Surf.* **125** (2020).
41. L Ping, C Narteau, Z Dong, Z Zhang, S Courrech du Pont, Emergence of oblique dunes in a landscape-scale experiment. *Nat. Geosci.* **7**, 99–103 (2014).
42. J Stout, T Zobeck, Intermittent saltation. *Sedimentology* **44**, 959–970 (1997).
43. J Ungar, P Huff, Steady state saltation in air. *Sedimentology* **34**, 289–299 (1987).
44. O Durán, P Claudin, B Andreotti, On aeolian transport: Grain-scale interactions, dynamical mechanisms and scaling laws. *Aeolian Res.* **3**, 243–270 (2011).
45. J Phillips, et al., Low-angle eolian deposits formed by protodune migration, and insights into slipface development at white sands dune field, new mexico. *Aeolian Res.* **36**, 9–26 (2019).
46. WS Cooper, *Coastal sand dunes of Oregon and Washington*. (Geological Society of America) Vol. 72, (1958).
47. G Kocurek, M Townsley, E Yeh, K Havholm, M Sweet, Dune and dune-field development on padre island, texas, with implications for interdune deposition and water-table-controlled accumulation. *J. Sedimentary Res.* **62**, 622–635 (1992).
48. B Andreotti, A Fourrière, F Ould-Kaddour, B Murray, P Claudin, Giant aeolian dune size determined by the average depth of the atmospheric boundary layer. *Nature* **457**, 1120–1123 (2009).
49. MC Baddock, JM Nield, GF Wiggs, Early-stage aeolian protodunes: Bedform development and sand transport dynamics. *Earth Surf. Process. Landforms* **43**, 339–346 (2018).
50. JM Davis, et al., Morphology, development, and sediment dynamics of elongating linear dunes on Mars. *Geoph. Res. Lett.* **47**, e2020GL088456 (2020).
51. C Cohen, M Berhanu, J Derr, SC du Pont, Buoyancy-driven dissolution of inclined blocks: Erosion rate and pattern formation. *Phys. Rev. Fluids* **5**, 053802 (2020).
52. M Bordiec, et al., Sublimation waves: Geomorphic markers of interactions between icy planetary surfaces and winds. *Earth-Science Rev.* **211**, 103350 (2020).
53. A Lucas, et al., Growth mechanisms and dune orientation on Titan. *Geophys. Res. Lett.* **41**, 6093–6100 (2014).
54. M Lapote, et al., Large wind ripples on mars: A record of atmospheric evolution. *Science* **353**, 55–58 (2016).
55. L Fernandez-Cascales, et al., First quantification of relationship between dune orientation and sediment availability, olympia undae, mars. *Earth Planet. Sci. Lett.* **489**, 241–250 (2018).
56. MW Telfer, et al., Dunes on pluto. *Science* **360**, 992–997 (2018).
57. RD Lorenz, Martian ripples making a splash. *J. Geophys. Res. Planets* **125**, e2020JE006658 (2020).
58. P Jia, B Andreotti, P Claudin, Giant ripples on comet 67p/churyumov–gerasimenko sculpted by sunset thermal wind. *Proc. Natl. Acad. Sci.* **114**, 2509–2514 (2017).

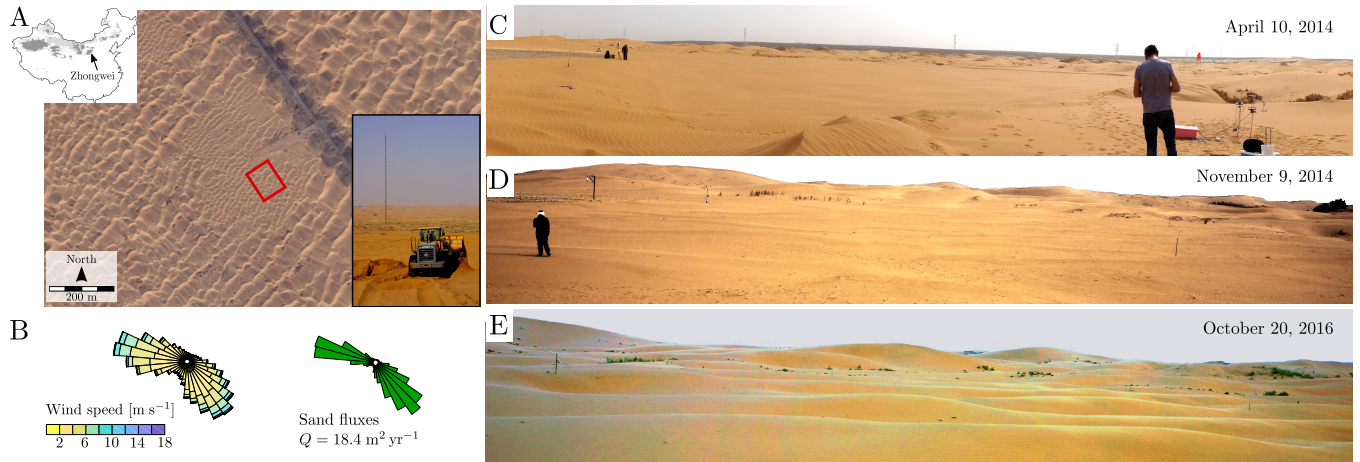


Fig. 1. A landscape-scale experiment on incipient dune growth. (A) The experimental site in the Tengger desert ($37^{\circ}33'38.14''\text{N}$, $105^{\circ}2'0.76''\text{E}$). The red square shows location of the flat sand bed experiment. (B) Wind and sand flux roses from January 2014 to November 2017. (C) View of the flat sand bed experiment in April 2014. (D) Incipient dunes at the end of the linear phase of dune growth in November 2014. (E) Mature dunes during the non-linear phase of dune growth in October 2016.

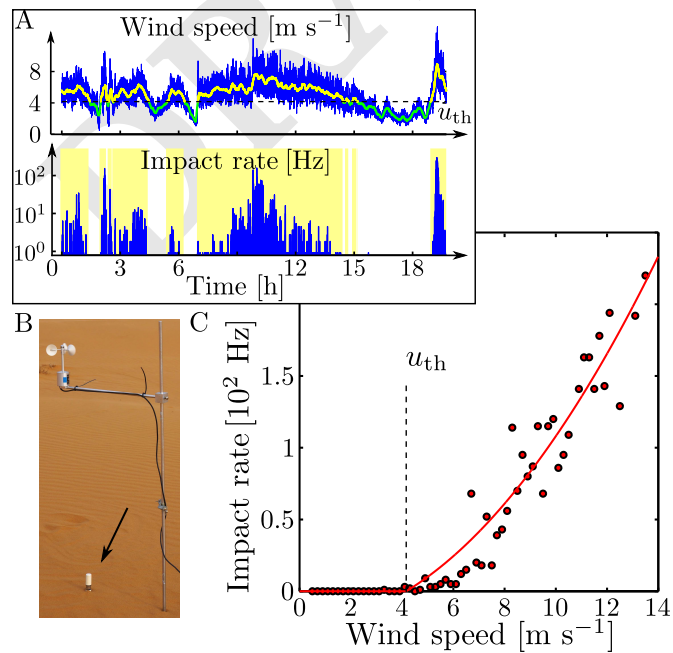


Fig. 2. The threshold wind speed for sand transport. (A) Grain impact rate and wind speed with respect to time. (B) Picture of the impact sensor placed above a flat sand and below a cup anemometer. (C) Relationship between grain impact rate and wind speed u measured at a height of 1.3 m. The solid line is the best fit of $(u^2 - u_{\text{th}}^2)$ to the data with a critical entrainment threshold $u_{\text{th}} = 4.16 \text{ m s}^{-1}$. Periods above the transport threshold are highlighted in yellow in Fig. 2A.

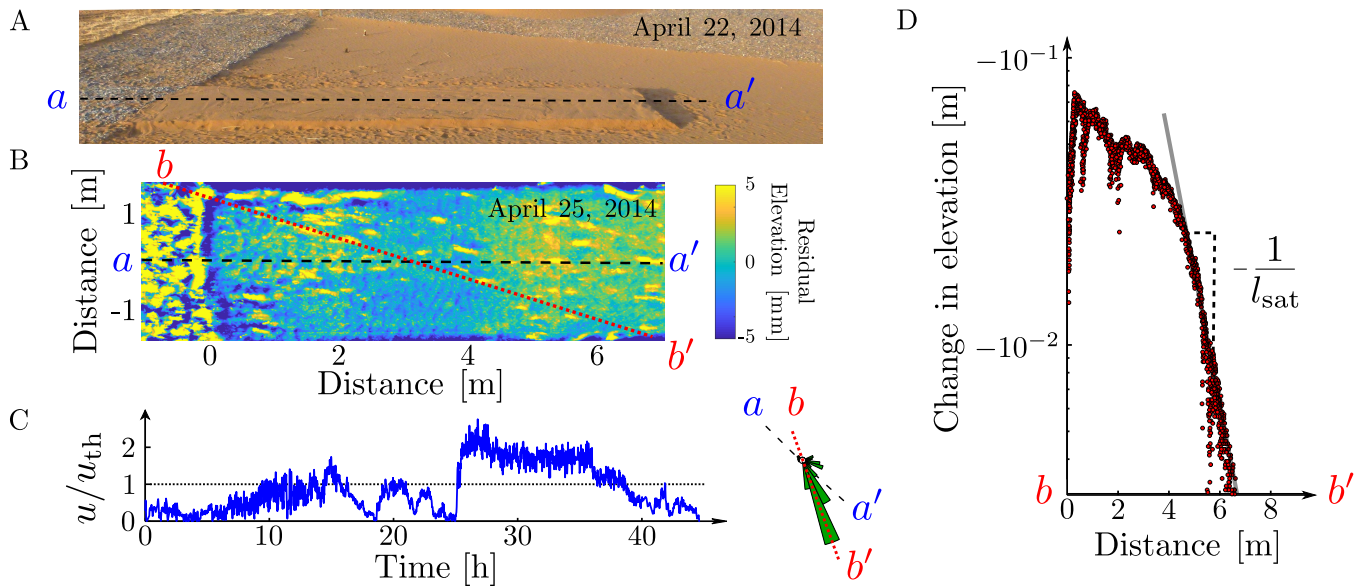


Fig. 3. The saturation length experiment. (A) The initial sand slab prepared and scanned on April 22, 2014. Placed downstream of a non-erodible bed composed of gravels, it has a length of 12 m, a width of 3 m and a main axis aa' aligned in the northwest-southeast direction, parallel to the orientation of the prevailing wind. (B) The residual elevation of the sand slab on April 25, 2014 after the passage of a storm event. It is the difference between the raw elevation map and a smoothed elevation map using a radius of 20 cm. (C) Wind speed and sand flux rose between the two scans. (D) Difference in surface elevation along the profile bb' between the two scans. Aligned with the resultant transport direction, this profile is selected from the orientation of ripples in B and the sand flux rose in C. The negative values show the net erosion along the entire profile, $\Delta H \sim -\exp(x/l_{\text{sat}})$. An exponential fit to the data gives $l_{\text{sat}} = 0.95$ m (Supplementary Information).

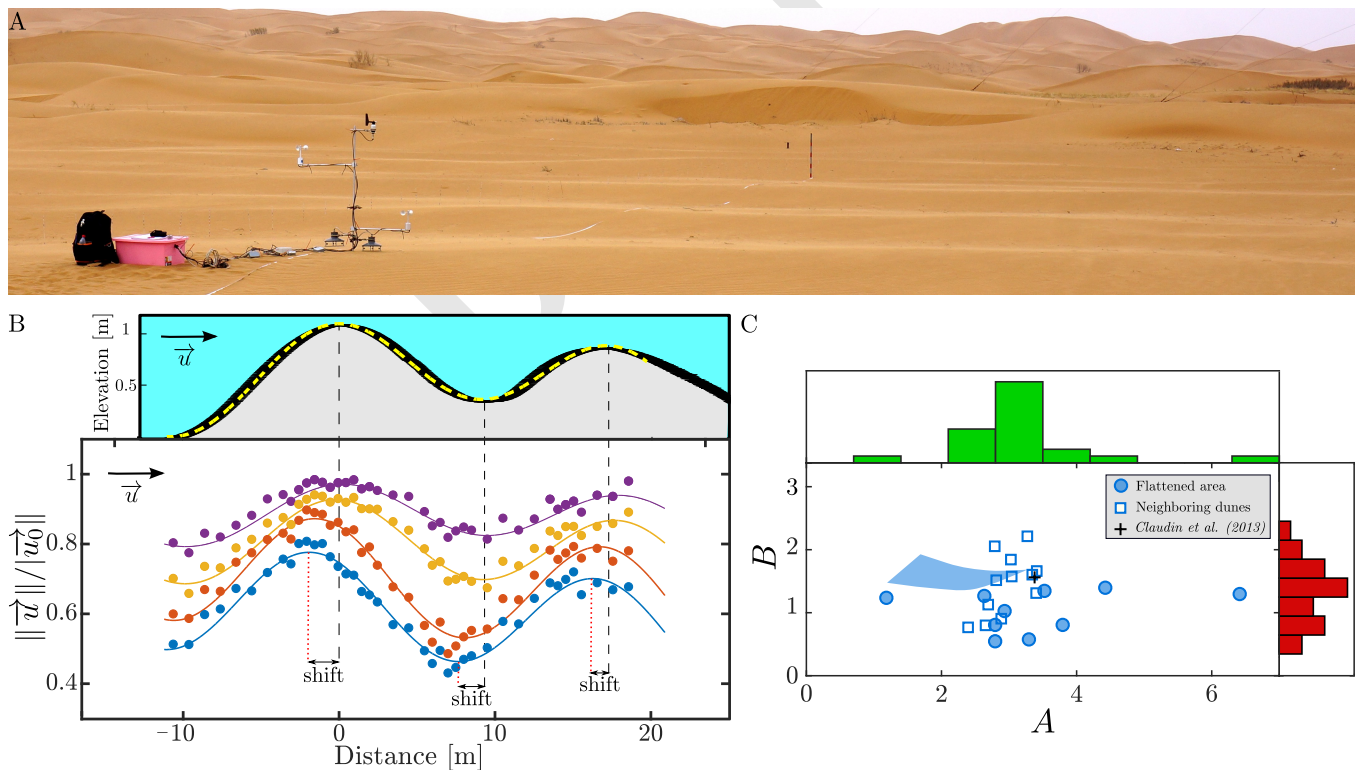


Fig. 4. The upwind velocity shift on low sinusoidal bedforms. (A) The mobile anemometer mast, with anemometers located at heights of 4 and 12 cm in the inner layer and at heights of 50 and 100 cm in the outer layer. The decameter aligned with the mean wind direction gives the direction followed during the successive measurements on sinusoidal incipient dunes. (B) Elevation and normalized wind speed according to distance along the dune profile (blue, red, yellow and purple for anemometers at 4, 12, 50 and 100 cm, respectively). The normalized wind speed is the wind speed measured along the profile divided by the one recorded by the reference anemometer. Note the upwind shift in wind speed in the inner layer near the bed, but not in the outer layer above. Dashed lines show the two dune crests and the trough along the elevation profile. Dotted lines show the maximum and minimum wind speed in the inner layer. (C) Values and distribution of aerodynamic parameters A and B measured during dune growth (circles) and on neighboring dunes (squares). The blue area shows the best fit values of A and B to the experimental dispersion relation shown in Fig. 6B for $0.6 < l_{\text{sat}} < 1.2$.

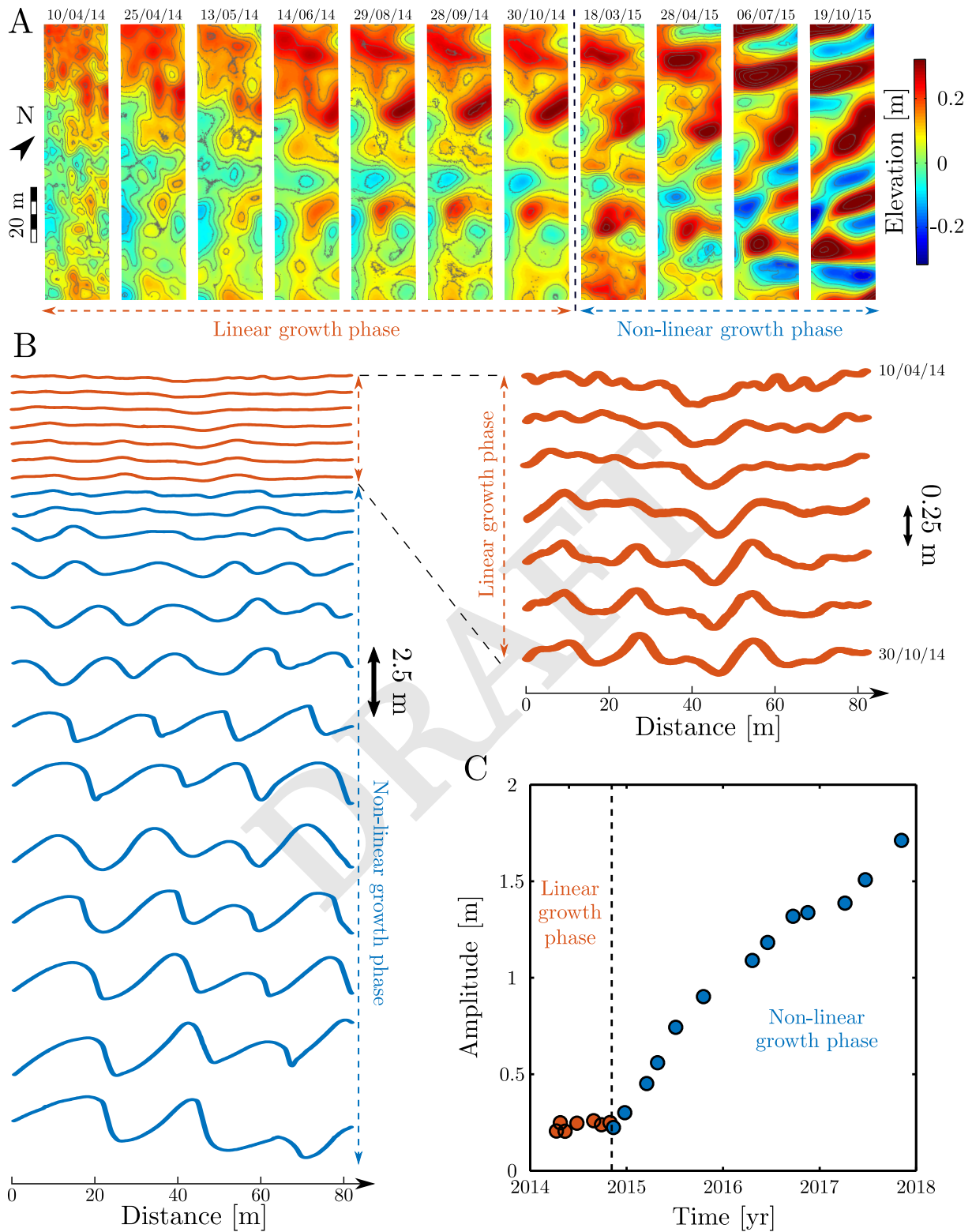


Fig. 5. Dune growth in the flat sand bed experiment. (A) Elevation maps during incipient dune growth from April 10, 2014 to October 19, 2015. (B) Detrended elevation profiles along the same transect from April 10, 2014 to November 7, 2017 obtained by averaging elevation data points over a 0.4 m wide band. Zooms on the elevation profiles from April 10, 2014 to October 30, 2014 show the evolution of topography during the linear phase of dune growth. (C) The mean amplitude $2\sqrt{2}(\langle h^2 \rangle - \langle h \rangle^2)^{1/2}$ of bedforms with respect to time. Colors and dashed lines are used to separate the linear (orange) and the non-linear (blue) phases of dune growth.

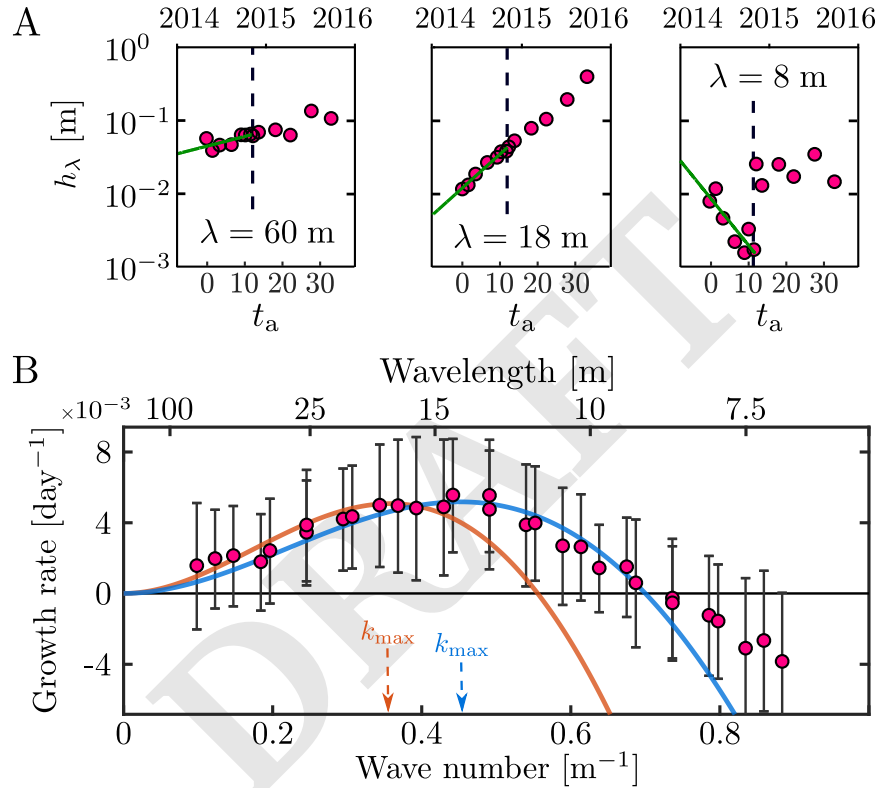


Fig. 6. The dispersion relation of the dune instability in the flat sand bed experiment. (A) Amplitude of 60, 18 and 8 m wavelengths with respect to the dimensionless transport time scale t_a ; t_a is set to 0 on April 10, 2014. Two different regimes are observed before and after $t_a = 10.7$, October 30, 2014 (dashed lines). There are associated with the linear and non-linear phases of dune growth. The growth rate of each wavelength (green lines) is determined by an exponential fit performed during the linear phase ($0 \leq t_a \leq 10.7$). (B) The experimental dispersion relation for the linear regime of the dune instability, i.e., the growth rate with respect to the wave number during the linear phase (dots). Errorbars show mean and standard deviation derived from the 34 independent transects. Solid lines are dispersion relations using Eq. 1 and the best fit to the data $\{l_{\text{sat}}, A, B\} = \{0.7, 1.96, 0.96\}$ (blue), or the same parameters measured independently in the field $\{l_{\text{sat}}, A, B\} = \{0.95, 3, 1.5\}$ (orange). The most unstable wavelengths $\lambda_{\text{max}} = 2\pi/k_{\text{max}}$ are equal to 14.6 and 18.5 m, respectively.

Direct validation of dune instability theory

— Supplementary Information —

Ping Lü^{1,*}, Clément Narteau^{2,*}, Zhibao Dong¹,
Philippe Claudin³, Sébastien Rodriguez², Zhishan An⁴,
Laura Fernandez-Cascales², Cyril Gadal², Sylvain Courrech du Pont⁵

¹ School of Geography and Tourism, Shaanxi Normal University, 620 Chang'an West Avenue, Xi'an, Shaanxi 710119, China.

² Université de Paris, Institut de physique du globe de Paris, CNRS, F-75005 Paris, France.

³ Physique et Mécanique des Milieux Hétérogènes, UMR 7636 CNRS, ES-PCI PSL Research Univ, Sorbonne Univ, Université de Paris, 10 rue Vauquelin, 75005 Paris, France.

⁴ Northwest Institute of Eco-Environment and Resources Donggang West Road 320, Lanzhou, Gansu Province 730000, China.

⁵ Laboratoire Matière et Système Complexes, Université de Paris. UMR 7057 CNRS, Bâtiment Condorcet, 10 rue Alice Domon et Léonie Duquet, 75205 Paris Cedex 13, France.

arXiv:2106.13117v1 [physics.geo-ph] 24 Jun 2021

*To whom correspondence should be addressed. E-mail: lvping@snnu.edu.cn, narteau@ipgp.fr

Contents

1	Supplementary Note 1	
	Wind data	3
2	Supplementary Note 2	
	Grain size distribution	3
3	Supplementary Note 3	
	Transport properties on a flat sand bed	4
4	Supplementary Note 4	
	Estimating the saturation length l_{sat} in the field	6
5	Supplementary Note 5	
	Upwind velocity shift at dune crests and troughs	9
	5.1 The inner and outer layers	9
	5.2 Measuring the upwind velocity shift within the inner layer	9
	5.3 From the upwind velocity shift to the hydrodynamic parameters A and B	11
6	Supplementary Note 6	
	Dispersion diagram from successive topographic surveys	12
	6.1 Aeolian dune formation as a linear instability	12
	6.2 The transition from the linear to the non-linear phases of dune growth	14
	6.3 A transport time scale for dune growth under variable wind strength	14
	6.4 Topographic surveys during experimental dune growth	18
	6.5 Spectral analysis, amplitude and phase	18
	6.6 Dispersion diagram of the growth rate	20
	6.7 Dispersion diagram of the phase velocity	22

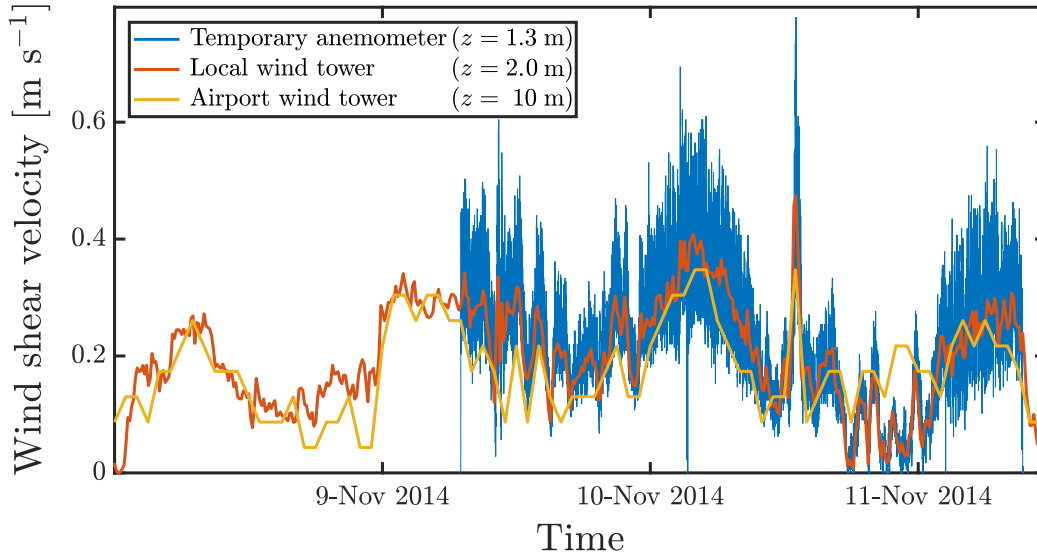


Figure S1: Comparison of wind speed data. Wind shear velocity derived from temporary wind speed measurements made during the threshold experiment (blue) and simultaneous measurements obtained on the local (red) and the airport wind towers (yellow). There is a general agreement between all these data sets.

1 Supplementary Note 1

Wind data

We installed a 2 m high wind tower in the center of our new experimental site and collected the wind data of the local airport located 10 km east. We use the local tower for the measurements of the transport threshold and the saturation length (see Figs. 2 and 3 of the main manuscript). We check the consistency between the local wind data and those collected at the airport. For the long-term experiment, we only use the wind data of the local airport.

Fig. S1 shows the shear velocity derived from a local wind measurement, the 2 m high wind tower and the airport meteorological tower during the transport threshold experiment (see Fig. 2 of the main manuscript). All these data are consistent with each other. As a consequence, the threshold shear stress derived from the local measurement can be extrapolated to other wind data to compute sand fluxes (Sec. 3).

2 Supplementary Note 2

Grain size distribution

The landscape-scale experiment site is located close to the oasis city of Shapotu at 8 km from the Yellow River in the Tengger Desert, which covers an area of about 36,700 km² in the northwest part of the Zhongwei County in the Ningxia Hui Autonomous Region of the People’s Republic of China (37° 31′ N, 105° E). This desert is characterized by a lognormal grain size distribution with a mean value $d=190 \mu\text{m}$ (Fig. S2).

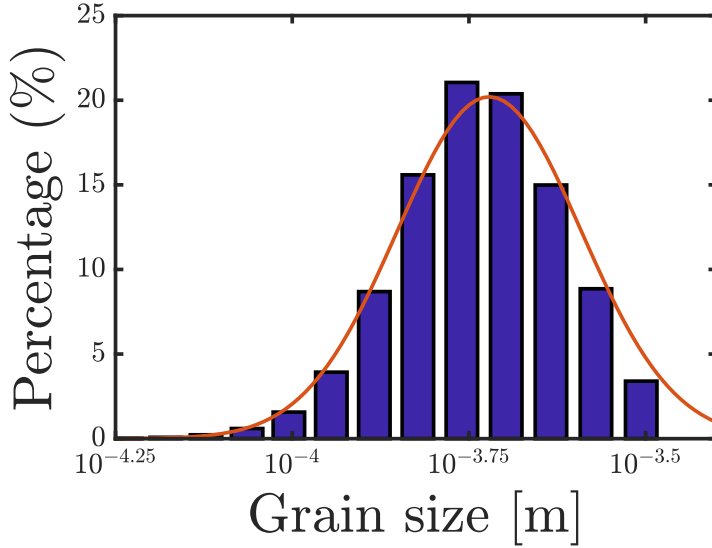


Figure S2: Grain size distribution in the Tengger Desert. The line is the best fit using a lognormal distribution with a mean value $d = 190 \mu\text{m} \approx 10^{-3.72} \text{ m}$.

3 Supplementary Note 3

Transport properties on a flat sand bed

Wind data are used to predict sand flux properties on a flat sand bed. Tab. S1 shows the results obtained using the formalism that follows.

Wind measurements provide the wind speed u_i and direction \vec{x}_i at different times t_i , $i \in [1; N]$. For each time step i , the shear velocity writes

$$u_*^i = \frac{u_i \kappa}{\log(z/z_s)}, \quad (1)$$

where z is the height at which the wind velocity u_i has been measured and κ the von-Kármán constant. Instead of the geometric roughness that depends only on grain size, we consider here the aerodynamic roughness z_s that accounts for the height of the transport layer in which saltating grains modify the vertical wind velocity profile. The value of the threshold shear velocity for motion inception is determined using the formula calibrated by *Iversen and Rasmussen*^[1]

$$u_{\text{th}} = 0.1 \sqrt{\frac{\rho_s}{\rho_f} g d}. \quad (2)$$

Using the gravitational acceleration g , the grain to fluid density ratio $\rho_s/\rho_f \simeq 2.05 \times 10^3$ and the grain diameter $d = 190 \mu\text{m}$, we find $u_{\text{th}} = 0.19 \text{ m s}^{-1}$, which corresponds to a threshold wind speed of $u_{10} = 4.4 \text{ m s}^{-1}$ ten meters above the ground. It is close to the values we measured in the field, which are $u_{\text{th}} = 0.23 \pm 0.04$ and $u_{10} = 5.3 \pm 0.92 \text{ m s}^{-1}$.

For each time step i , the saturated sand flux \vec{Q}_i on a flat sand bed is computed from the relationship proposed by *Ungar and Hauff*^[2] and calibrated by *Durán et al.*^[3]

$$Q_{\text{sat}}(u_*) = \begin{cases} 25 \frac{\rho_f}{\rho_s} \sqrt{\frac{d}{g}} (u_*^2 - u_{\text{th}}^2) & \text{for } u_* > u_{\text{th}}, \\ 0 & \text{else.} \end{cases} \quad (3)$$

In this formula, the prefactor takes into account a dune compactness of 0.6.

Variable	Units	Value
Acceleration of gravity g	m s^{-2}	9.81
Grain size d	m	190×10^{-6}
Air density ρ_f	kg m^{-3}	1.29
Grain density ρ_s	kg m^{-3}	2.55×10^3
Aerodynamic roughness z_s	m	10^{-3}
von-Kármán constant κ	\emptyset	0.4
Shear velocity and sand flux on a flat sand bed		
Threshold shear velocity u_{th}	m s^{-1}	0.19
Mean shear velocity $\langle u_* \rangle$	m s^{-1}	0.29
$\langle u_* \rangle / u_{\text{th}}$	\emptyset	1.5
DP = $\langle \ \vec{Q}\ \rangle$	$\text{m}^2 \text{ yr}^{-1}$	18.4
RDP = $\ \langle \vec{Q} \rangle\ $	$\text{m}^2 \text{ yr}^{-1}$	5.7
RDP/DP	\emptyset	0.32
RDD	mod 360°	266.6

Table S1: Shear velocity and sand fluxes derived from the airport wind data from January 1, 2013 to October 31, 2017. The wind and sand flux roses are shown in Fig. 1B of the main manuscript. See text and Eqs. 1-9 for the description of all the variables. The resultant drift direction (RDD) is measured counterclockwise from East.

From the individual saturated sand flux vectors \vec{Q}_i , we estimate the mean sand flux vector on a flat erodible bed

$$\langle \vec{Q} \rangle = \sum_{i=2}^N \vec{Q}_i \delta t_i / \sum_{i=2}^N \delta t_i, \quad (4)$$

where $\delta t_i = t_i - t_{i-1}$. The norm of the mean sand flux is usually called the resultant drift potential:

$$\text{RDP} = \|\langle \vec{Q} \rangle\|. \quad (5)$$

This quantity is highly dependent on the wind regime. Since it is a vectorial sum, the contributions of winds from opposite directions cancel each other out. For the entire time period, we also calculate the drift potential,

$$\text{DP} = \sum_{i=2}^N \|\vec{Q}_i\| \delta t_i / \sum_{i=2}^N \delta t_i. \quad (6)$$

Unlike the resultant drift potential, this mean sand flux does not take into account the orientation of the individual sand fluxes computed from the successive wind measurements^[4].

The ratio RDP/DP is a non-dimensional parameter, which is often used to characterize the directional variability of the wind regimes^[5, 6]: RDP/DP \rightarrow 1 indicates that sediment transport tends to be unidirectional; RDP/DP \rightarrow 0 indicates that most of the transport components cancel each other. Finally, RDD is the resultant drift direction, i.e., the direction of $\langle \vec{Q} \rangle$.

The mean shear velocity $\langle u_* \rangle$ is defined as the shear velocity averaged over the transport periods. i.e. when $Q_{\text{sat}} > 0$. Using the Heaviside function $H_{u_{\text{th}}}$ defined as

$$H_{u_{\text{th}}} = \begin{cases} 1 & \text{for } u_* > u_{\text{th}}, \\ 0 & \text{else.} \end{cases} \quad (7)$$

the mean shear velocity can be defined directly from the shear velocity

$$\langle u_* \rangle = \frac{\sum_{i=2}^N H_{u_{\text{th}}}^i u_*^i}{\sum_{i=2}^N H_{u_{\text{th}}}^i}, \quad (8)$$

or from the integrated flux using the inverse function Q_{sat}^{-1} of the transport law (Eq. 3)

$$\langle u_* \rangle = Q_{\text{sat}}^{-1} \left(\text{DP} \times \frac{\sum_{i=2}^N \delta t_i}{\sum_{i=2}^N H_{u_{\text{th}}}^i \delta t_i} \right). \quad (9)$$

These two estimations of $\langle u_* \rangle$ are close to each other considering wind data from the Tengger Desert.

4 Supplementary Note 4

Estimating the saturation length l_{sat} in the field

Let us consider an infinite flat granular bed under a unidirectional wind in a statistically steady state. Eventually, the transport rate reaches an equilibrium state due to the negative feedback between the density of moving grains and the strength of the flow, which determines the saturated flux Q_{sat} (Eq. 3). We consider now a situation for which the flow and the sediment flux is non-homogeneous or unsteady in space or time. The actual flux q does not immediately adjust to the local value of the shear stress^[7, 8, 9]. It needs some space and time to reach its equilibrium Q_{sat} -value (Fig. S3). Over bedforms, the transport is never far from its saturated state, so it can be expressed by a first-order linear relaxation in both space and time

$$t_{\text{sat}} \frac{\partial q}{\partial t} + l_{\text{sat}} \frac{\partial q}{\partial x} = q_{\text{sat}} - q, \quad (10)$$

where l_{sat} and t_{sat} are the saturation length and the saturation time, respectively^[8, 10, 11]. The t_{sat} -value is usually much smaller (≈ 1 s) than the characteristic time scale for the evolution of the bed ($\approx 10^5$ s). Such a separation in scale justifies the simplifying assumption that the fluid flow and sediment transport can be considered and computed as if the bed was fixed^[3]. Neglecting t_{sat} , the saturation transient described by Eq. 10 has been successfully applied to the description of dune formation^[9, 11, 10, 12, 13]. Under the configuration shown in Fig. S3, we have

$$q(x) = Q_{\text{sat}} \left(1 - \exp \left(- \frac{x - x_0}{l_{\text{sat}}} \right) \right). \quad (11)$$

In practice, the saturation length l_{sat} scales as $(\rho_s/\rho_f)d$ the distance needed for one grain to be accelerated up to the wind velocity^[10, 14, 15, 16]:

$$l_{\text{sat}} \approx 2.2 \frac{\rho_s}{\rho_f} d, \quad (12)$$

As shown in Fig. S4 and in Fig. 3 of the main manuscript, we determine the value of l_{sat} from the evolution of the topography of a rectangular sand pile placed downstream of a non-erodible bed composed of gravels. We thus have the experimental setup that best reflects the theoretical conditions presented in Fig. S3. The rectangular sand pile has a length of 12 m and a width of

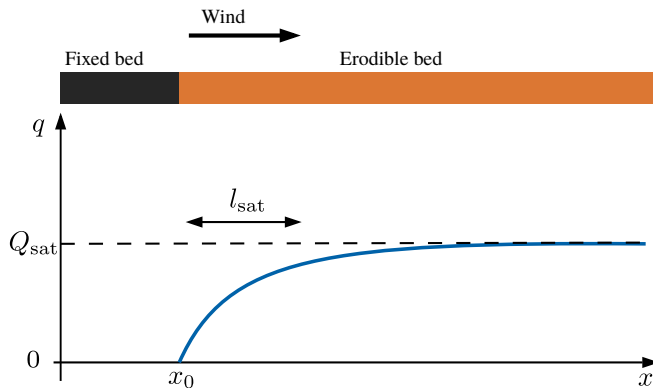


Figure S3: A schematic representation of the saturation length experiment. The saturation length may be described as the relaxation length of the sand flux q toward its saturated value Q_{sat} . The experiment set-up is a flat sand bed preceded by a flat non-erodible bed. When the wind blowing over this rigid surface reaches the erodible bed, the sand flux relaxes exponentially towards its saturation value Q_{sat} over a characteristic distance l_{sat} in the direction of the flow.

3 m with its main axis aligned in the northwest-southeast direction, parallel to the orientation of the prevailing wind (Fig. S4a). The initial sand pile was prepared and scanned on April 22, 2014 (Fig. S4b). A storm occurred on April 24 with winds from the north-northwest and irregular wind speeds reaching 15 m s^{-1} at a height of 2 m. The sand pile was scanned again on April 25 (Fig. S4c).

Considering the ideal assumption of our initially flat surface under a steady wind of constant direction, strength and transport rate q , Eq. 11 can be combined with the equation of conservation of mass to estimate the erosion rate

$$\frac{\partial h(x)}{\partial t} = -\frac{\partial q(x)}{\partial x} = -\frac{Q_{\text{sat}}}{l_{\text{sat}}} \exp\left(-\frac{x-x_0}{l_{\text{sat}}}\right). \quad (13)$$

This equation can be integrated to estimate the net erosion over a given time period. In this case the exponential regime is expected to hold. However, it cannot be observed from the start of the erodible bed for several reasons, both theoretical and experimental. The main reasons are related to (1) the natural variability of wind speed and direction and (2) the development of a discontinuity in the topographic profile between the non-erodible and the erodible beds. In addition, Eq. 13 neither takes into account the possible dependence of l_{sat} on wind speed^[17], nor the spatial shift associated with the establishment of a transport layer when the sand flux starts from zero^[16].

Using the field data and despite the number of simplifying assumptions, we study the difference in height ΔH between the two surface elevations to look for zones where

$$\Delta H \sim -\exp(x/l_{\text{sat}}). \quad (14)$$

In practice, we use 2D elevation profiles aligned with the primary sand transport direction during the storm. It forms an angle of 22° with the orientation of the initial sand pile. This angle is estimated from the sand flux rose as well as from the orientation of ripples and accretion mounds (Fig. S4c).

The slope of the exponential decay in Eq. 14 gives the value of l_{sat} (Fig. 3D of the main manuscript). We find a value of 0.95 m from our field data, a value that can be directly compared to the 0.83 m predicted by Eq. 12 and the parameters given in Tab. S1.

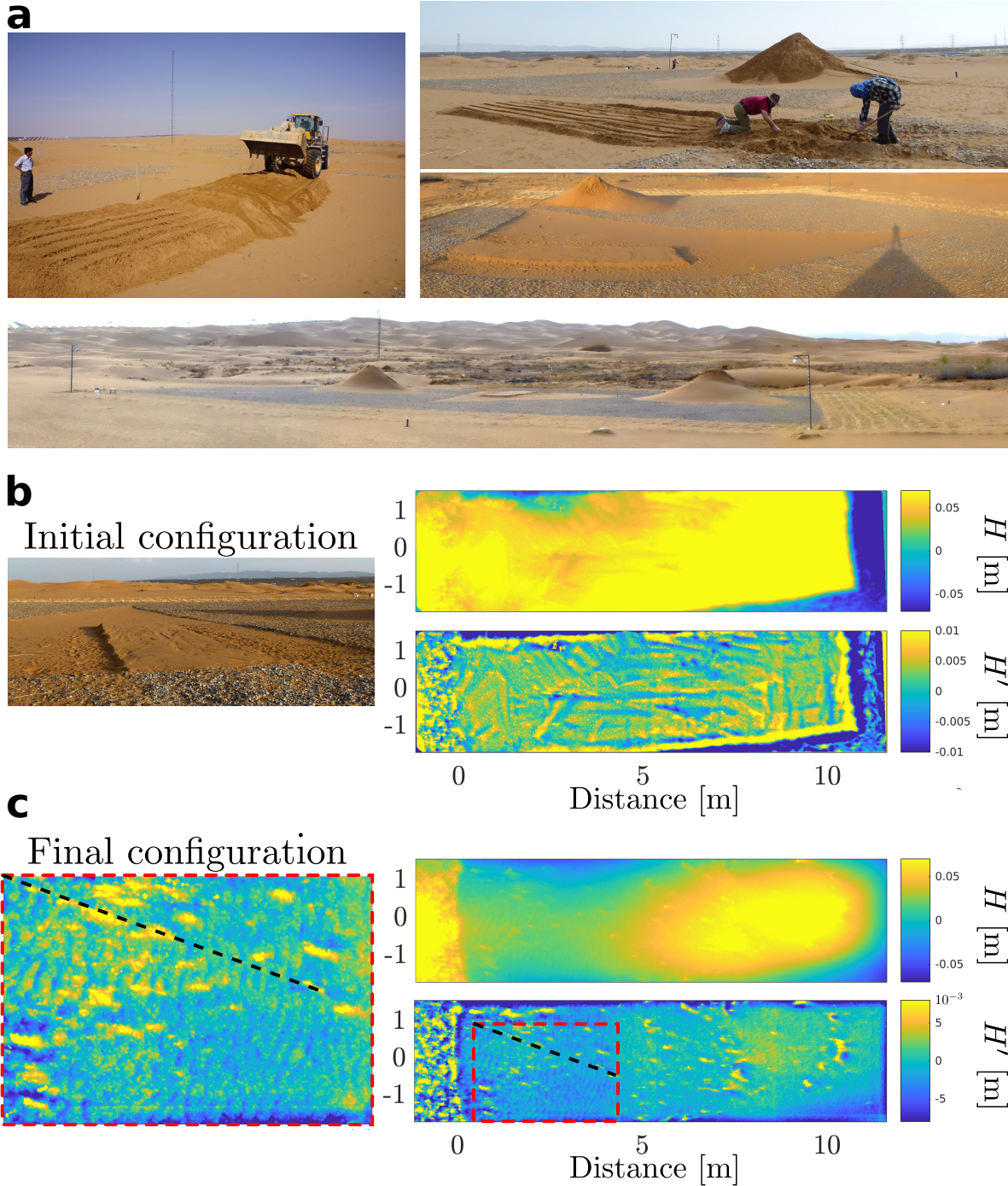


Figure S4: Measuring the saturation length l_{sat} in the field. (a) Setting up the l_{sat} experiment between the two sand piles of the elongating dune experiment in a triangular area of bare sand within a flat bed armored with gravels. In this area, a rectangular sand pile 12 m long and 3 m wide is placed downstream of the non-erodible gravel bed. The long axis is aligned along the northwest-southeast direction, the orientation of the prevailing wind. The sand bed is flattened so that there is no vertical step between the erodible and non-erodible zones. (b) Elevation of the rectangular sand pile on April 22, 2014 before aeolian transport. (c) Elevation of the rectangular sand pile on April 25, 2014 after the passage of a northwestern depression (see flux rose in Fig. 3C of the main manuscript). H is the absolute elevation from a base level. H' is the difference of elevation with a smoothed surface obtained using a sliding window with a radius of 20 cm. The inset in c show the transect along which the elevation profile used to estimate l_{sat} has been extracted (see Fig. 3B of the main manuscript). It is parallel to the sand deposits that form downwind of topographic obstacles and perpendicular to aeolian ripples.

5 Supplementary Note 5

Upwind velocity shift at dune crests and troughs

5.1 The inner and outer layers

Flows that are topographically forced by obstacles (e.g., hills or sand dunes) accelerates on the upwind slopes and decelerates on the downwind slopes. Then, in order to study sediment transport over a dune, we should first describe some properties of the turbulent flow over an undulating topography. Conceptually, as proposed by *Jackson and Hunt (1975)*^[18] in the limit of small amplitudes bedforms, the turbulent flow over a sinuous bed elevation profile of wavelength λ can be decomposed into two layers:

- The outer layer is the external region (supposed infinite) where the pressure gradient set up by the topography is balanced by the inertial forces. The streamlines follow the topography. At a given height, the wind speed is maximum (minimum) above the top (bottom) of the topography. The amplitude of the perturbation vanishes on a characteristic height that varies according to the wavelength of the topography. Then, sufficiently far above the obstacle, the wind speed is finally equal to the undisturbed wind speed in the absence of topography (see Eq. 1).
- The inner layer is a zone in which the longitudinal pressure gradient exerted by the fluid is compensated by the Reynolds shear stress induced by the turbulent motions at the surface of the bed. Then, the pressure gradient is in phase quadrature with the topography and is maximum where the stoss slope is steepest. Hence, there is an upwind velocity shift within the inner layer. The characteristic thickness l of the inner layer depends on both the wavelength of the bed elevation profile and on the aerodynamic roughness z_s so that^[18, 19]

$$\frac{l}{\lambda} \log^2 \left(\frac{l}{z_s} \right) = 2\kappa^2. \quad (15)$$

For typical value of the aerodynamic roughness ($z_s < 10^{-2}$ m) and wavelengths of hundreds of meters, the inner layer is always confined in a meter scale envelop above the topography. For $\lambda = 20$ m and $z_s = 10^{-3}$ m, common values observed during the development of aeolian bedforms under high wind speed, the inner layer is less than 20 cm.

5.2 Measuring the upwind velocity shift within the inner layer

A sufficiently strong wind and a stable wind orientation are essential for the quality of the measurements. The sequence of measurements consists in moving an anemometer mast upwind along a given profile of known elevation. The entire procedure to estimate the upwind velocity shift on dunes is described in full details in *Claudin et al. (2013)*^[20]. We follow here the same procedure with the specifications detailed below.

We performed our measurements on low dunes with sinusoidal shape. The density of measurements is high near the crests and troughs (≈ 20 cm) but lower in the steeper sections (≈ 1 m).

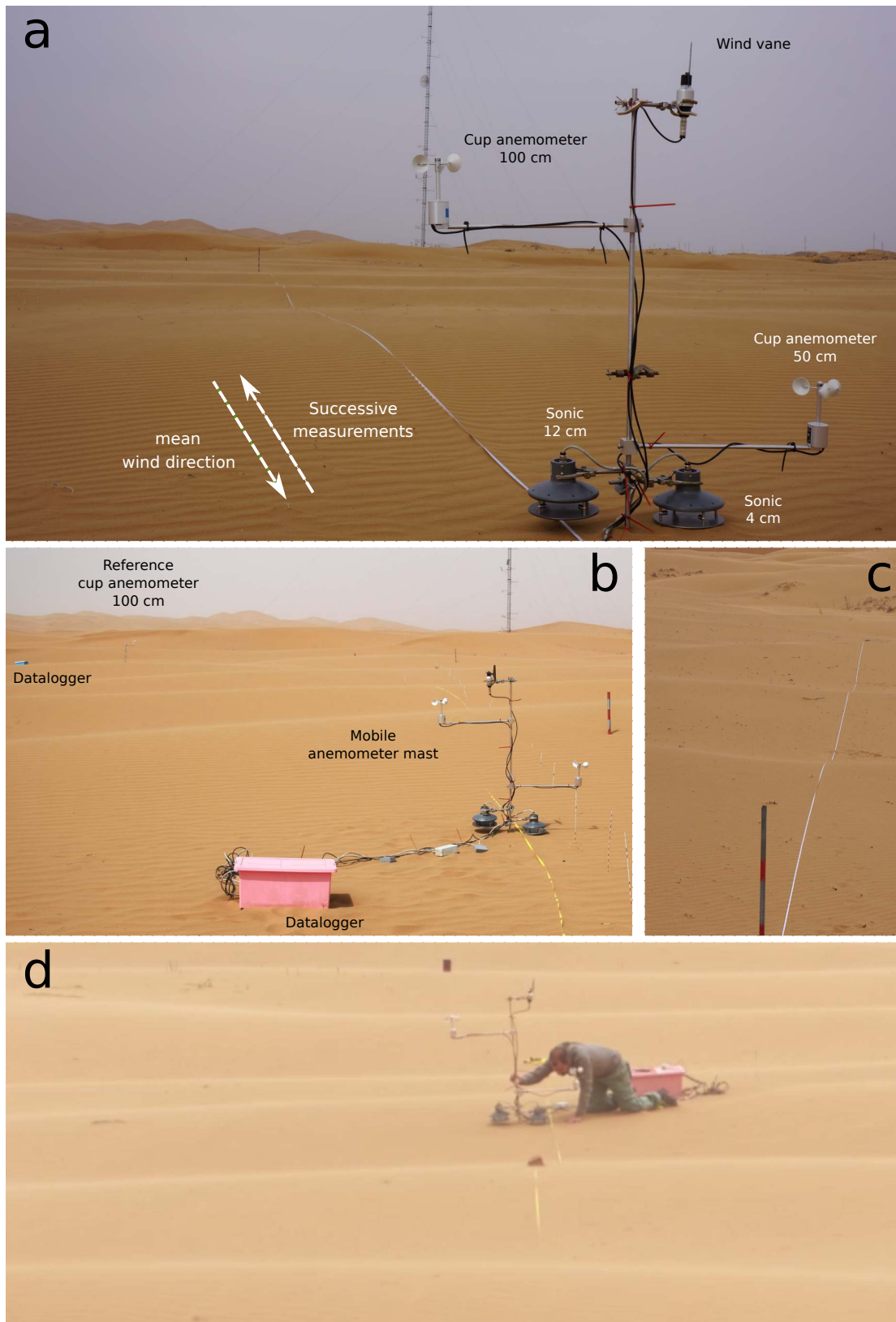


Figure S5: Experimental set-up to estimate the upwind velocity shift at the crests and troughs of incipient dunes. (a) The mobile anemometer mast, with anemometers located at heights of 4 and 12 cm in the inner layer and at heights of 50 and 100 cm in the outer layer. Arrows show the mean wind direction and the measurement path. (b) The anemometer mast and the reference anemometer. (c) A measurement path perpendicular to the crest orientation of the bed instability. (d) Setting a new measurement for 10 min with a sampling frequency of 1 Hz.

Each measurement lasts 10 min with a sampling frequency of 1 Hz. The mobile anemometer mast has sonic anemometers located at heights of 4 and 12 cm and cup anemometers at heights of 50 and 100 cm (Fig. S5a). Given the natural variability in wind speed between two measurements, the wind speeds measured along the mobile mast are normalized by the wind speed measured at one meter high by a reference cup anemometer located at the top of a larger dune in the vicinity (Fig. S5b). The normalized wind speeds along the profile can then reveal how sensitive is the flow to topography at different heights. As shown in Fig. 4B of the main manuscript, in the limit of small sinusoidal oscillations, the wind profiles at all heights reflect the topography, i.e., the spatial variation of the wind speed exhibits the same wavelength as the bedforms. Most importantly for our present purposes, the flow is in phase with the topography at heights of 50 and 100 cm and in phase advance at heights of 4 and 12 cm. It indicates that the inner layer has a thickness between 12 and 50 cm, a range of value that covers entirely the values given by Eq. 15 for aeolian dune systems on Earth.

5.3 From the upwind velocity shift to the hydrodynamic parameters A and B

On several occasions during our field campaigns, we have measured wind velocity in the inner and outer layers on a succession of crests and troughs to estimate the phase shift over more than a wavelength of the dune pattern (Fig. S5c,d). Here, we focus only on individual dune crests or troughs, which are approximated by

$$H(x) = H_{\text{ref}} + h \cos(kx), \quad (16)$$

where k is the wave number (wavelength $\lambda = 2\pi/k$), h the amplitude. The position of the dune crests and troughs are set at $x = 0$ and $x = \lambda/2$, respectively. The arbitrary reference level H_{ref} is here chosen such that $H > 0$. Fitting Eq. 16 to the dune elevation data gives the values of k and h . The dune aspect ratio is $R = 2h/\lambda = hk/\pi$. When the aspect ratio is below $\simeq 0.05$, we expect that the (low) perturbation calculation of the aerodynamics to be valid. A more refined analysis would involve the computation of the Fourier transform of the dune profile, in order to account for a whole range of wave numbers k .

Alike topography, the wind profile at a given height along the dune can also be fitted by a sinusoidal function of the same wave number k as for the dune elevation:

$$u_b(x) = u_b^0 + \delta u_b \cos(kx + \varphi_b). \quad (17)$$

As said in Sec. 5.1, the topography $Z(x)$ and the wind velocity $u_b(x)$ are not in phase for anemometers at heights of 4 and 12 cm: the velocity reaches its maximum upstream of the crest. Here the phase difference is φ_b so that the upwind velocity shift in the inner layer is φ_b/k . The two other fitting parameters are u_b^0 and δu_b .

Because the logarithmic law of the wall (Eq. 1) locally holds in the inner layer at each position x , the velocity can be used as a proxy to calculate the basal shear stress with $\tau_b \propto \rho_f u_b^2$. By expansion to the first order, we can then write:

$$\tau_b(x) \propto \rho_f (u_b^0)^2 (1 + kh (A \cos(kx) - B \sin(kx))), \quad (18)$$

where A and B are given by

$$A = 2 \times \frac{\delta u_b}{u_b^0} \times \frac{\cos(\varphi_b)}{kh} \quad \text{and} \quad B = 2 \times \frac{\delta u_b}{u_b^0} \times \frac{\sin(\varphi_b)}{kh}. \quad (19)$$

Eqs. 18 and 19 are specific to the quadratic relation between τ_b to u_b . Since sediment transport is controlled by the basal shear stress, these two parameters A and B are all that are needed as aerodynamical inputs in bedform evolution models. As described in the introduction of the main manuscript, they are of fundamental importance for the understanding of the mechanisms of dune growth and dune size-election (see also Sec. 6 and Eqs. 23-24). Tab. S2 shows the results obtained in April and November 2015 in our experiment. We observe no significant trend in the variation of A and B during dune growth.

6 Supplementary Note 6

Dispersion diagram from successive topographic surveys

Dispersion relations are plotted as growth rate σ and phase velocity c with respect to wave number k . They are used in linear stability analysis to identify the most unstable wavelength, which is likely to be observed. We describe here how we measure the growth rate of dunes as a function of their wave numbers k from successive topographic surveys throughout the duration of our experiment. Before, we present the rationale for studying dune formation as a linear instability in a landscape scale experiment.

6.1 Aeolian dune formation as a linear instability

In what follows, the term instability characterizes the growth of a small perturbation in a system, which is often considered to be as homogeneous and simple as possible. Conversely, stability refers to the ability of this system to return to its original state when perturbed. The main objective of stability analysis is to identify the ranges of perturbation wavelengths over which the system exhibits stable or unstable behavior. Quantitative approaches consist of estimating the initial growth rate of each mode (wavelength) considering that all these modes are independent of each other. Obviously, the highest and zero growth rates are particularly important. The highest ones are associated with the most unstable modes, which will have the greatest impact on the system. Those at zero are neutral modes that often mark the transition between stable and unstable regimes.

The analysis of the time and length scales of instabilities by means of linearized equations is a standard approach in hydrodynamics and many other branches of physics. By identifying stabilizing and destabilizing mechanisms, these linear stability analyses reveal how they together govern the evolution of the system over the entire range of possible wavelengths. During the first stage of the instability (the linear regime), the initial wavelength λ_g of the perturbation is assumed to stay constant, whereas its amplitude h grows exponentially with time

$$h(k_g, t) \propto \exp(\sigma(k_g)t). \quad (20)$$

Variable	Units	Description								
Topography										
λ	m	dune wavelength								
k	m^{-1}	Dune wave number								
h	m	Amplitude of the dune								
R	\emptyset	Dune aspect ratio								
Flow										
δu_b	m s^{-1}	Amplitude of wind speed variation in the inner layer.								
u_b^0	m s^{-1}	Mean wind speed in the inner layer.								
φ_b	$^\circ$	Phase shift between the flow and the topography in the inner layer.								
Hydrodynamic parameters										
A	\emptyset	In-phase hydrodynamic parameter								
B	\emptyset	In-quadrature hydrodynamic parameter								
14/04	15/04	15/04*	15/04	16/04	18/04	03/11	03/11*	03/11	15/11	
Topography										
λ	14.84	18.57	10.50	16.45	21.92	14.51	25.05	14.49	21.06	14.33
k	0.423	0.338	0.598	0.382	0.287	0.433	0.251	0.437	0.298	0.439
h	0.297	0.262	0.185	0.414	0.358	0.338	0.662	0.323	0.264	0.361
R	0.020	0.014	0.018	0.025	0.016	0.023	0.026	0.022	0.012	0.025
Flow										
δu_b	0.126	0.111	0.108	0.198	0.0624	0.143	0.306	0.134	0.132	0.174
u_b^0	0.683	0.650	0.656	0.678	0.743	0.701	0.568	0.622	0.739	0.661
φ_b	25.51	11.89	15.95	20.79	45.95	10.92	11.36	19.13	17.42	9.80
Hydrodynamic parameters										
A	2.648	3.770	2.860	3.453	1.138	2.737	6.362	2.906	4.328	3.278
B	1.264	0.794	0.817	1.311	1.176	0.528	1.278	1.008	1.358	0.566

Table S2: Topography and wind measurements carried out in April and November 2015. Measurements on dune troughs are shown with a * on April 4 and November 3, 2015. They are located between two dune crests along the same transect to estimate the phase shift over more than one wavelength of the dune pattern.

In this expression, $k_g = 2\pi/\lambda_g$ is the wave number and $\sigma(k_g)$ the growth rate with units of frequency. Positive and negative growth rates correspond to unstable and stable modes, respectively. The dispersion relation $\sigma(k)$ gives the growth rate value of the perturbation as a function of the wave number k . The largest positive σ -value corresponds to the most unstable mode $\{k_{\max}, \lambda_{\max}\}$. Zero values corresponds to neutral modes $\{k_0, \lambda_0\}$. In diffusive systems, dispersion relations are often characterized by a transition from a stable to an unstable regime. for an increasing wavelength. In other words, $\sigma(k) > 0$ for $k < k_0$ and $\sigma(k) < 0$ for $k > k_0$. Beyond the linear stage of the instability, when the amplitude of the initial perturbation is too high, the dispersion relation no longer applies because the different modes interact with one another. It is described as the non-linear stage of the

instability.

Here, we study the formation of aeolian dunes as a linear instability. More exactly, we focus on the dependence and feedback between bed forms, wind flow and sand transport properties. The governing equations lead to the theoretical expression of a dispersion relation as a function of the different physical parameters of the system (see Eq. 1 of the main manuscript). Thus, the minimum size for dunes is associated with a neutral mode and a transition from unstable to stable regime for decreasing wavelength. The emergence and growth of periodic dune patterns are associated with a most unstable mode which is going to prevail within the whole dune field. Based on observation of mature aeolian dunes in nature, previous studies have measured the wavelength and the migration rate of dunes in order to derive values of λ_0 , λ_{\max} and σ_{\max} under various conditions. Dispersion relations have been given less attention or even disregarded, certainly because of the length and time scales involved in the mechanism of aeolian dune growth. Then, a direct validation of the dune instability theory is to investigate whether or not dispersion diagrams can be derived from field data. Another solution is to verify whether the theoretical formalism used with the values of the underlying physical parameters measured independently in the field is actually capable of accurately predicting the observations.

Here, we apply this methodology to the formation of dunes in a landscape scale experiment. Our initial system is a sand bed after flattening by a bulldozer. In such an experimental set up, but also in all natural dune environments, there are always heterogeneities and defects at all length scales and our initial condition already contains all the perturbation wavelengths.

6.2 The transition from the linear to the non-linear phases of dune growth

The continuous transition from the linear to the non-linear phases of dune growth is controlled by dune aspect-ratio, which is the main control parameter for aerodynamic non-linearities. Figs. S6a-b show the elevation and slope maps during incipient dune growth in our experimental field from April 10, 2014 to July 6, 2015. There is a significant change in slope maps between October 30 and November 12, 2014. Over this time interval, the local slopes not only become steeper, they also become spatially organized, just like dune crest, to form more regular transverse structures across the flattened area. This occurs for a mean slope of about 0.03 (Fig. S6c) at the same time as incipient slip faces a few centimeter high emerge (Fig. S7). The mean slope $\langle \|\vec{\nabla}H\| \rangle$ variations can be compared to the amplitude of the bedforms in Figs. S6b-c. Based on these observations, we set the transition between October 30 and November 12, 2014. This transition is not spontaneous but it is surely completed in April 2015, when the mean slope reaches a value of about 0.07.

6.3 A transport time scale for dune growth under variable wind strength

In order to quantify dune growth under variable wind strength, it is necessary to define a new time scale that accounts for the intensity of transport. For example, periods during which there is no transport should not be used as time increments, while storm periods should contribute more to the total time.

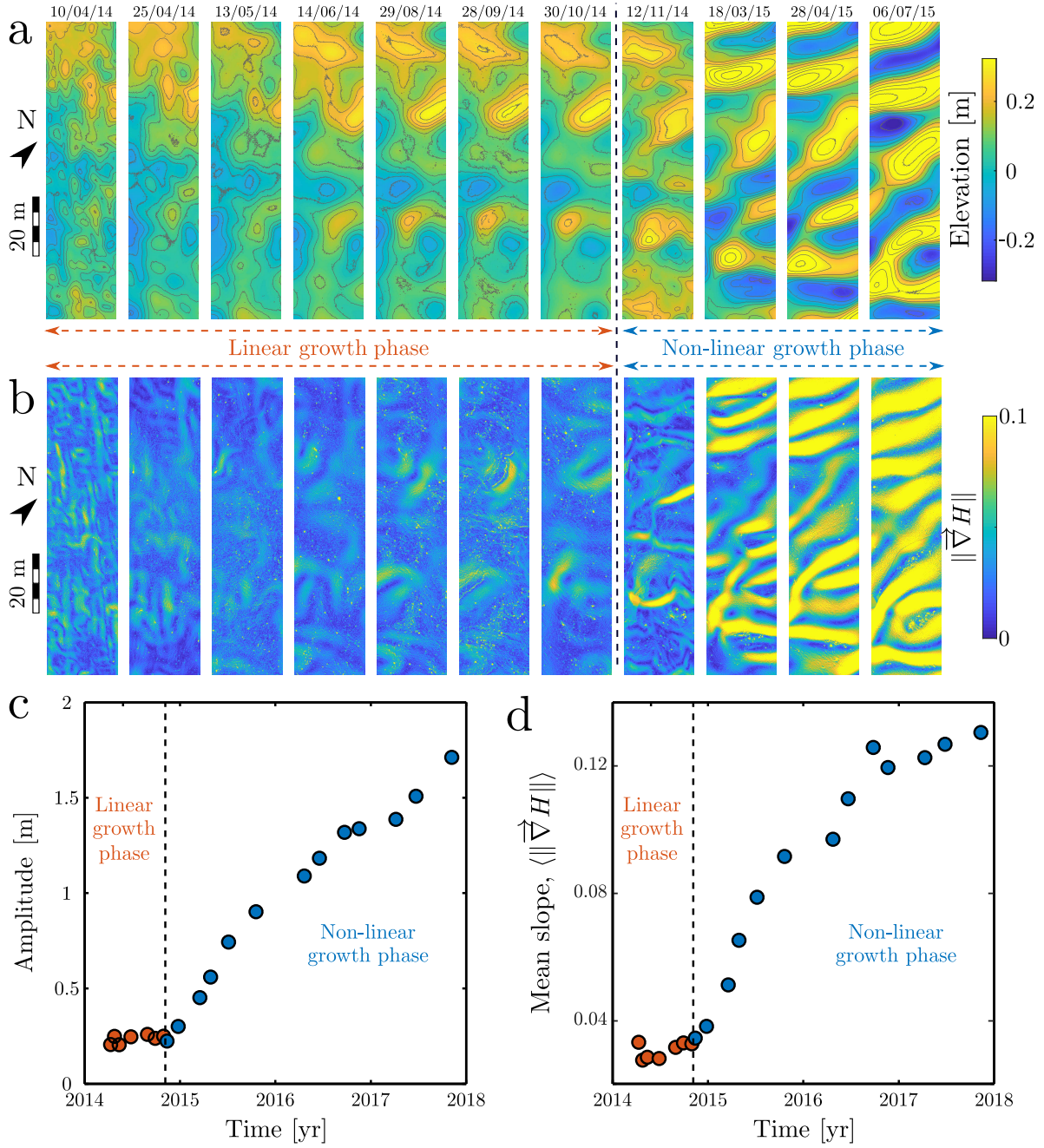


Figure S6: The transition from the linear to the non-linear phases of dune growth. (a) Elevation and (b) slope maps during incipient dune growth from April 10, 2014 to July 6, 2015. The colormap in Fig. S6b is saturated to distinguish the slopes of bedforms in fall 2014, around the transition from the linear to the non-linear phases of dune growth. In non-saturated areas, ripples can be observed. A cable crosses the experimental field from 28 April 2015. (c) The mean amplitude $2\sqrt{2}(\langle h^2 \rangle - \langle h \rangle^2)^{1/2}$ of bedforms and (d) the mean slope $\langle \|\hat{\nabla}H\| \rangle$ with respect to time. The higher mean slope value on April 10, 2014, after the flattening, is due to bulldozer tracks that can be seen in Fig.S6b. Colors and dashed lines are used to separate the linear (orange) and the non-linear (blue) phases of dune growth. For comparison with slope data, Fig. S6d is the same as Fig. 5C of the main manuscript.



Figure S7: Bedforms during the transition from the linear to the non-linear phases of dune growth. (a) Incipient slip faces a few centimetres high on November 6, 2014. (b) Periodic dune patterns on November 10, 2014. This pictures can be compared to elevation and slope maps of October 30, 2014 and November 12, 2014 shown in Fig. S6a and S6b.

In practice, the new time scale is defined sequentially from the wind data using the saturated sand flux (Eq. 3) and the saturation length l_{sat} . Starting at $t = 0$ at the flattening time, the new times write

$$t_a(t) = \frac{\sum_{i=1}^t \|\vec{Q}_i\| \delta t_i}{l_{\text{sat}}^2}. \quad (21)$$

This time scale is dimensionless allowing for comparison across different time series and various time periods. Using the saturated sand flux derived from the local wind data (Eq. 3), Fig. S8 shows the dimensionless times with respect to time from April 10, 2014 to October 31, 2017 using the saturation length $l_{\text{sat}} = 0.95$ m measured in the field (Fig. 3 of the main manuscript). By definition, periods of stronger winds are associated with steeper slopes, and vice versa. The choice of the characteristic length for the computation of the dimensionless transport time scale, (here l_{sat}) is of minor significance since we consider it to be constant.

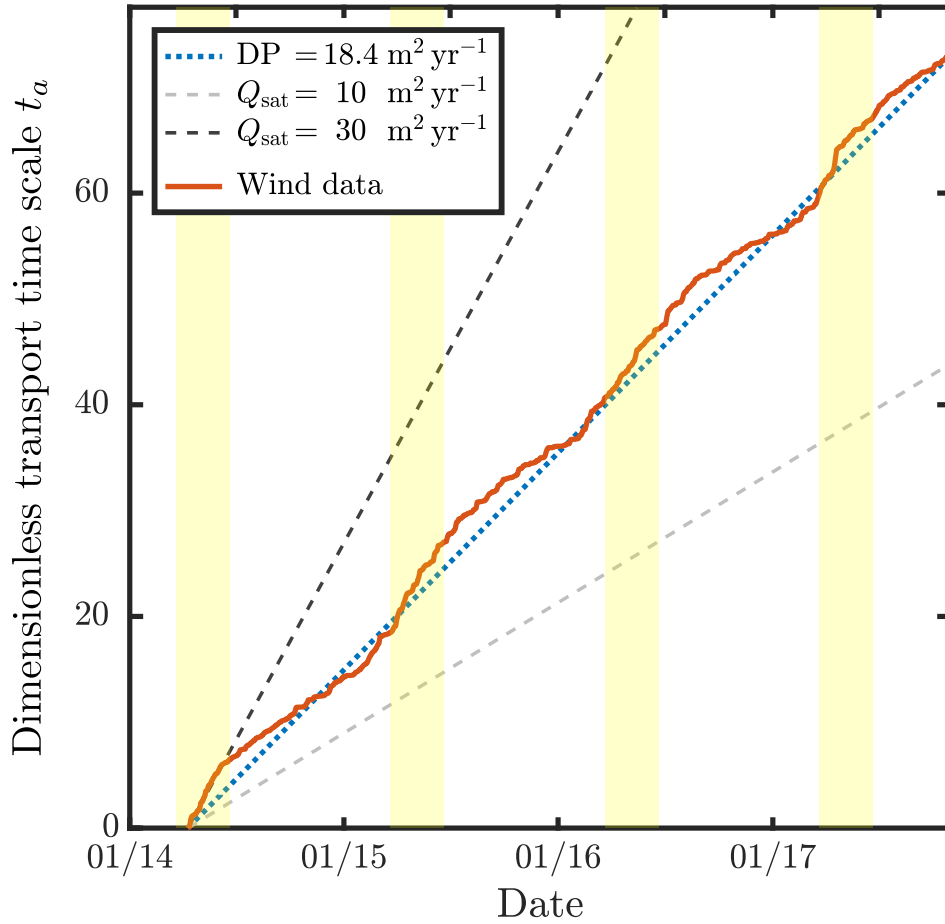


Figure S8: A dimensionless transport time scale for dune growth under variable wind strength. Using the saturated sand flux derived from wind data (Eq. 3), the red solid line shows the dimensionless transport time scale t_a as a function of time from April 10, 2014, when the dune field was flattened. By definition, the mean slope is given by the RDP (blue line, Eq. 5). Light and dark gray lines show the transport time scale for constant sand fluxes of 10 and 30 $\text{m}^2 \text{yr}^{-1}$, respectively. Highlighted areas show the spring periods from March 21 to June 21.

6.4 Topographic surveys during experimental dune growth

From April 2014 to November 2017, we performed a series of topographic surveys of the dunes developing from the flat sand bed using a ground-based laser scanner Leica Scanstation C10 (Fig. S9a). To compare these different measurements, a reference system of concrete posts was installed over the entire experimental dune field (Figs. S9b-d). For each survey, the zone under investigation is scanned from four different view points. Over the 42 months of the experiment, the density of points varies from 472 to 2368 points/m².

To map surface elevation, we select only elevation points within the 4-sided polygon determined by reference points t6, t7, t8 and t9 (Figs. S9c-d). Within this polygon, to avoid disturbances from the surrounding bedforms, we have chosen a central rectangular area with a width of 48 m and a length of 82 m (ABCD in Figs. S9c-d). The long side of this rectangle is oriented Northwest-Southeast to align perpendicular to the final orientation of the dunes at the end of the experiment. We remove the mean slope of this rectangular area by adjusting a plane to the elevation data. This plane has always a southwest-facing slope during the entire duration of the experiment. The residual topography is shown for different times in Fig. 5A of the main manuscript. Within the rectangular area, we study 2D transects parallel to the main axis using a spacing of 1.4 m between two transects (see for example transect aa' in Figs. S9c-d). For each of the 34 transects, we select the elevation data points in a 0.2 m wide band on either side. All these points are horizontally projected on their respective transect line. After subtracting the average slope and the mean elevation, we resample these data to a regular spacing of 0.1, 0.25 and 0.35 m. Thus, we can use the fast Fourier transform method to explore different values within the frequency domain.

Fig. 5B of the main manuscript shows the elevation profiles with respect to time for the transect aa' shown in Figs. S9c-d. Over the 42 months of the experiment, the amplitude of the dunes varies from a few centimeters to a few meters.

6.5 Spectral analysis, amplitude and phase

For each transect and all topographic surveys, we use a fast Fourier transform method to analyze the signal in the frequency domain (Figs. S10a,b). By selecting only one frequency value, the individual contribution of each wavelength is computed by an inverse Fourier transform (Fig. S10c). Thus, we obtain a sine wave

$$H_{\lambda_i}^j(t_n) = h_{\lambda_i}^j(t_n) \cos(k_i x + \phi_{\lambda_i}^j(t_n)) \quad (22)$$

for each wavelength $\lambda_i = 2\pi/k_i$ of each transect j at the different times t_n of the n^{th} topographic survey. Considering the 34 different transects, the amplitude h and the phase ϕ can be used to estimate growth rates σ_{λ_i} and phase velocities c_{λ_i} with respect to time, respectively. We perform this analysis on the same elevation profiles sampled at different rates (0.1, 0.25 and 0.35 m) to verify that it has no effect on the spectral behavior.

Taking as an example transect N^o 20 in the middle of the selected area, Fig. S11 shows the logarithm of the amplitude A_{λ}^{20} of individual wavelengths with respect to the dimensionless time

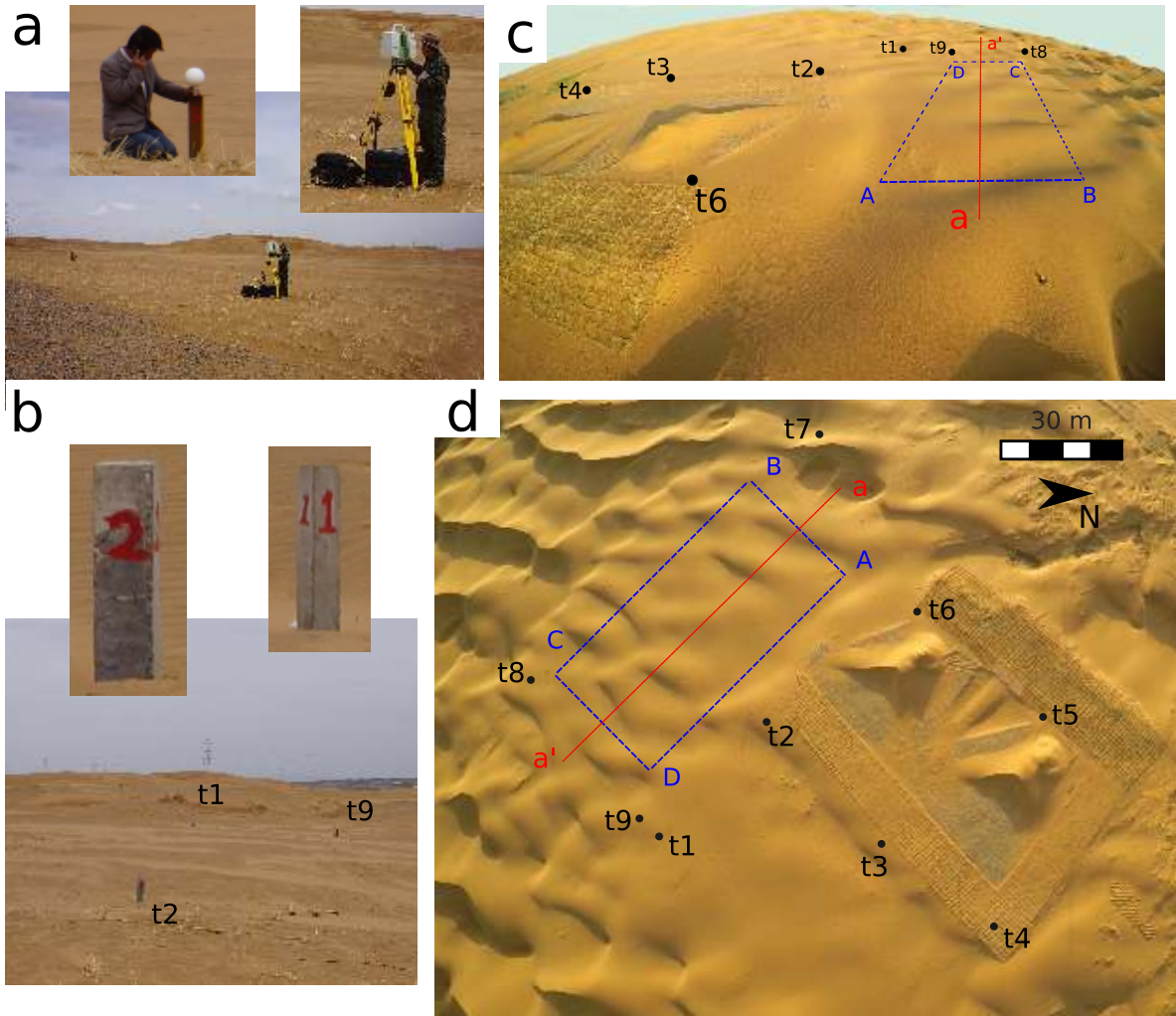


Figure S9: Topographic surveys during experimental dune growth. (a) Ground laser scanning in the landscape-scale experiment. (b) Ground view of three posts of the local reference system. (c,d) Reference system (dots) and selected area (blue rectangle) for the entire duration of the experiment. All 2D elevation profiles are taken parallel to the transect aa' (red line). They are separated by a distance of 1.4 m. The elevation profiles of the same transects at different times are used to study the dune instability.

scale. A sudden change in behavior is observed between $t_a = 10.7$ and $t_a = 11.3$, i.e. from October 30 to November 12, 2014. Over this time period, there is an abrupt increase in growth rate and then a more irregular behavior than during the initial phase. As shown in Fig. 5C of the main manuscript, it is also during this period that the mean amplitude of the bedforms begins to increase more rapidly. These behaviors are interpreted as the transition between linear and non-linear growth phases. This interpretation is supported by the observation of the first slip faces downwind of the crest under the prevailing wind.

In order to quantify dune growth in the linear phase according to the dune instability (see Sec. 6.1 and Eq. 20), we perform an exponential fit to the amplitude data from $t_a = 0$ to $t_a = 10.7$, i.e. from April 10 to October 30, 2014, for each wavelength and each transect (see red lines in Fig. S11). The agreement between the exponential regime and the data as well as the variation of the exponential rate at different wavelengths indicate that there is a coherent behavior at different length scales, which can be analyzed thanks to a dispersion diagram.

6.6 Dispersion diagram of the growth rate

Fig. S11 shows the dispersion relation for transect N°20 during the linear phase from $t_a = 0$ to $t_a = 10.7$, i.e. from April 10 to October 30, 2014. In this figure, the exponential rates of growth or decay of the different wavelengths λ_i are plotted with respect to the wave number $k_i = 2\pi/\lambda_i$. From the longest wavelengths (i.e. smallest wave numbers), there is an increase in the growth rate. The maximum growth rate is reached for $k_{\max} \approx 0.43 \text{ m}^{-1}$ ($\lambda_{\max} \approx 14.6 \text{ m}$). For shorter wavelengths, the growth rate is decreasing and the neutral mode is reached for a value of k_0 of about 0.67 m^{-1} ($\lambda_c \approx 9.3 \text{ m}$). Then, shorter wavelengths have negative growth rates. These decay rates are associated with small amplitudes of less than one centimeter, so that their rapid variations can not be captured given the resolution of our topographic data.

Fig. S12a shows the dispersion relations of the growth rate for all transects and the three sampling rates. The mean and standard deviation of these growth rates are plotted with respect to the wave number in Fig. S12b. Using these data, we find $k_{\max} \approx 0.45 \text{ m}^{-1}$ ($\lambda_{\max} \approx 14 \text{ m}$) and $k_c \approx 0.7 \text{ m}^{-1}$ ($\lambda_c \approx 9 \text{ m}$).

Theoretically, the growth rate writes

$$\sigma(k) = Q k^2 \frac{B - A k l_{\text{sat}}}{1 + (k l_{\text{sat}})^2} \quad (23)$$

where A and B are the aerodynamic parameters (Sec. 5), l_{sat} the saturation length (Sec. 4), Q a constant flux proportional to u_*^2 . This equation does not take into account the transport threshold and is therefore theoretically valid only within the limit of strong winds when the sand flux is large. However, the role of the transport threshold is included in our estimates thanks to the dimensionless time scale and a prefactor correcting for the intensity of the sand flux. In practice, the growth rate derived from the elevation profiles scales as $\sigma(k)/Q$ and we consider a prefactor $\langle u_* \rangle^2 / (\langle u_* \rangle^2 - u_{\text{th}}^2)$ that integrates all the variations of wind strength. Thus, the parameter A and B in Eq. 18 and in Eq. 23 are compatible with one another.

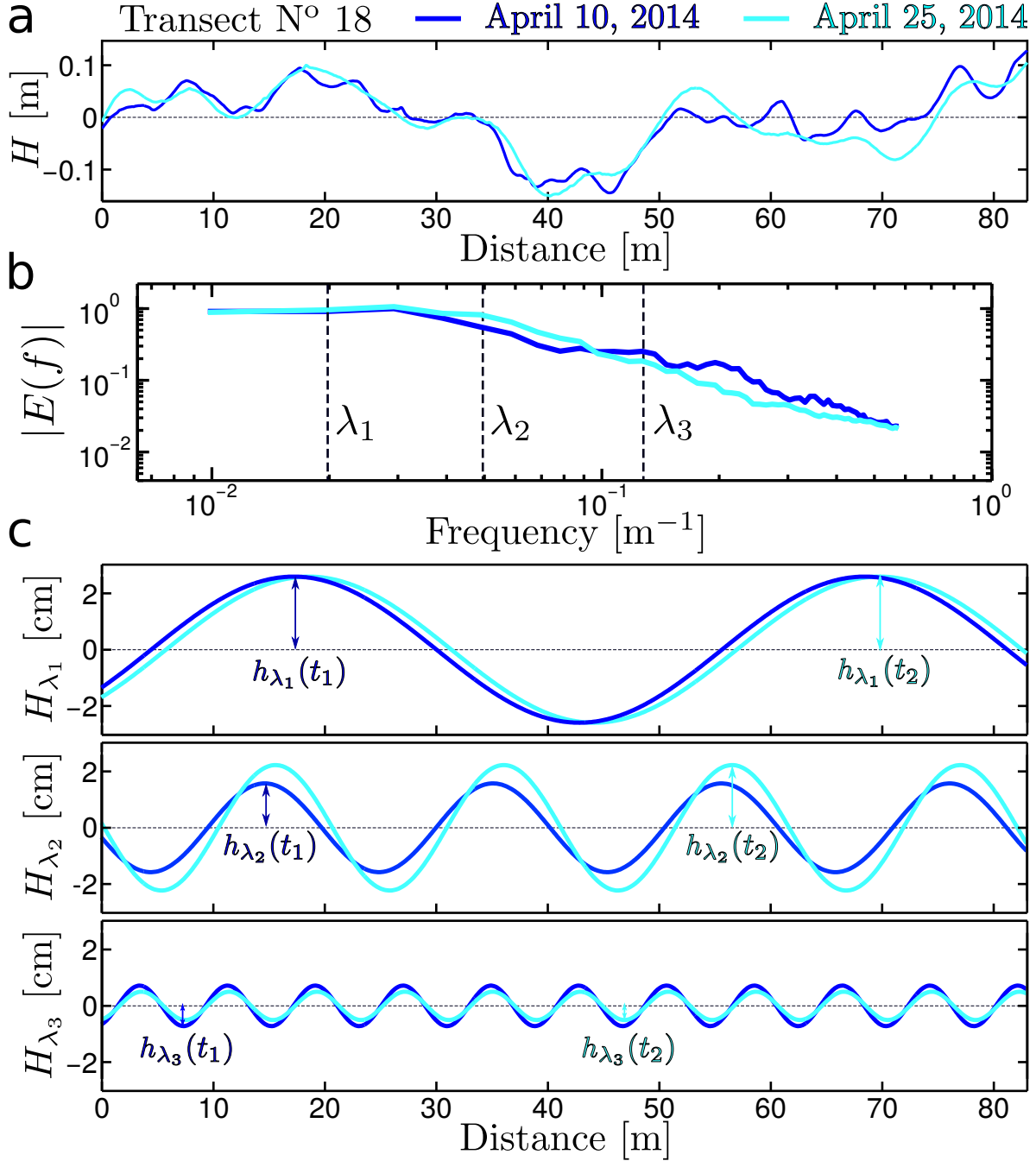


Figure S10: Spectral analysis of elevation profiles with respect to time. (a) Two consecutive elevation profiles of transect N° 18 during dune growth. (b) Power spectral density of the elevation profiles using a fast Fourier transform. Dashed lines show wavelengths $\lambda_{\{1,2,3\}}$ of $\{51.2, 20.5, 7.9\}$ m. (c) The reconstructed elevation profiles using individual wavelengths $\lambda_{\{1,2,3\}}$ and the inverse Fourier transform. By definition, they take the form of sine waves $H_{\lambda_i} = h_{\lambda_i} \cos(k_i x + \phi_{\lambda_i})$ where $k_i = 2\pi/\lambda_i$ is the wave number and ϕ_{λ_i} the phase. Values of h_{λ_i} and ϕ_{λ_i} at different times can be used to estimate growth rate σ_{λ_i} and phase velocity c_{λ_i} , respectively.

The dispersion relation using Eq. 23 and the values of $\{l_{\text{sat}}, A, B\} = \{0.95, 3, 1.5\}$ measured independently in the field are plotted in orange in Figs S11 and S12 as in Fig. 6B of the main manuscript. The blue curve in these figures corresponds to a dispersion relation with the best-fit values of $\{l_{\text{sat}}, A, B\} = \{0.7, 1.96, 0.96\}$. In addition, to investigate the sensitivity of the dispersion relation to the values of $\{l_{\text{sat}}, A, B\}$, the shaded area in Fig. 3c of the main manuscript shows the best-fit values of A and B using values of $l_{\text{sat}} \in [0.5; 1.1]$ in Eq. 23. All these results underline the consistency of the experimental dispersion diagram derived from the topographic data not only with the theory but also with our independent measurements of flow and transport properties in the field.

6.7 Dispersion diagram of the phase velocity

During the linear-growth phase, the analysis of the variation of the phase $\phi(\lambda_i)$ (Eq. 22) as a function of time do not at present provide conclusive evidence about the dispersion diagram of the phase velocity. An obvious limitation comes from the time delay between two consecutive topographic surveys. Indeed, the phase shift can be too large to be accurately computed, even by folding the data modulo the period from large to short wavelengths. The orientation and magnitude of the resultant sand flux associated with each time interval is another obvious issue. In fact, wind reversals and the subsequent back and forth of the incipient bedforms were frequent during the experiment. Variation of the phase data during periods of strong winds and small resultant sand flux are particularly difficult to be interpreted.

To simplify the problem, we can also estimate dune migration distance by cross correlation between two elevation profiles over a time interval over which the wind is almost unidirectional, from April 25 to May 13, 2014, (Figs. S13a,b). The dune migration rate can then be computed using the dimensionless time scale to be compared to theoretical dispersion relations. With the same notation as in Eq. 23, dispersion relations write

$$c(k) = Qk \frac{A + Bk l_{\text{sat}}}{1 + (k l_{\text{sat}})^2}. \quad (24)$$

Considering the dimensionless time scale and the same prefactor as for the growth rate, Fig. S13c shows the dispersion relations of the phase velocity using the same parameters as in Figs. S11 and S12. It also shows the phase velocity of the most unstable wavelength λ_{max} , the mean value of the migration rate averaged over all transects and the corresponding standard deviation. As expected, the migration rate derived from the cross correlation is close to the phase velocity of the most unstable wavelength.

References

- [1] Iversen, J. D. & Rasmussen, K. R. The effect of wind speed and bed slope on sand transport. *Sedimentology* **46**, 723–731 (1999).
- [2] Ungar, J. & Haff, P. Steady state saltation in air. *Sedimentology* **34**, 289–299 (1987).

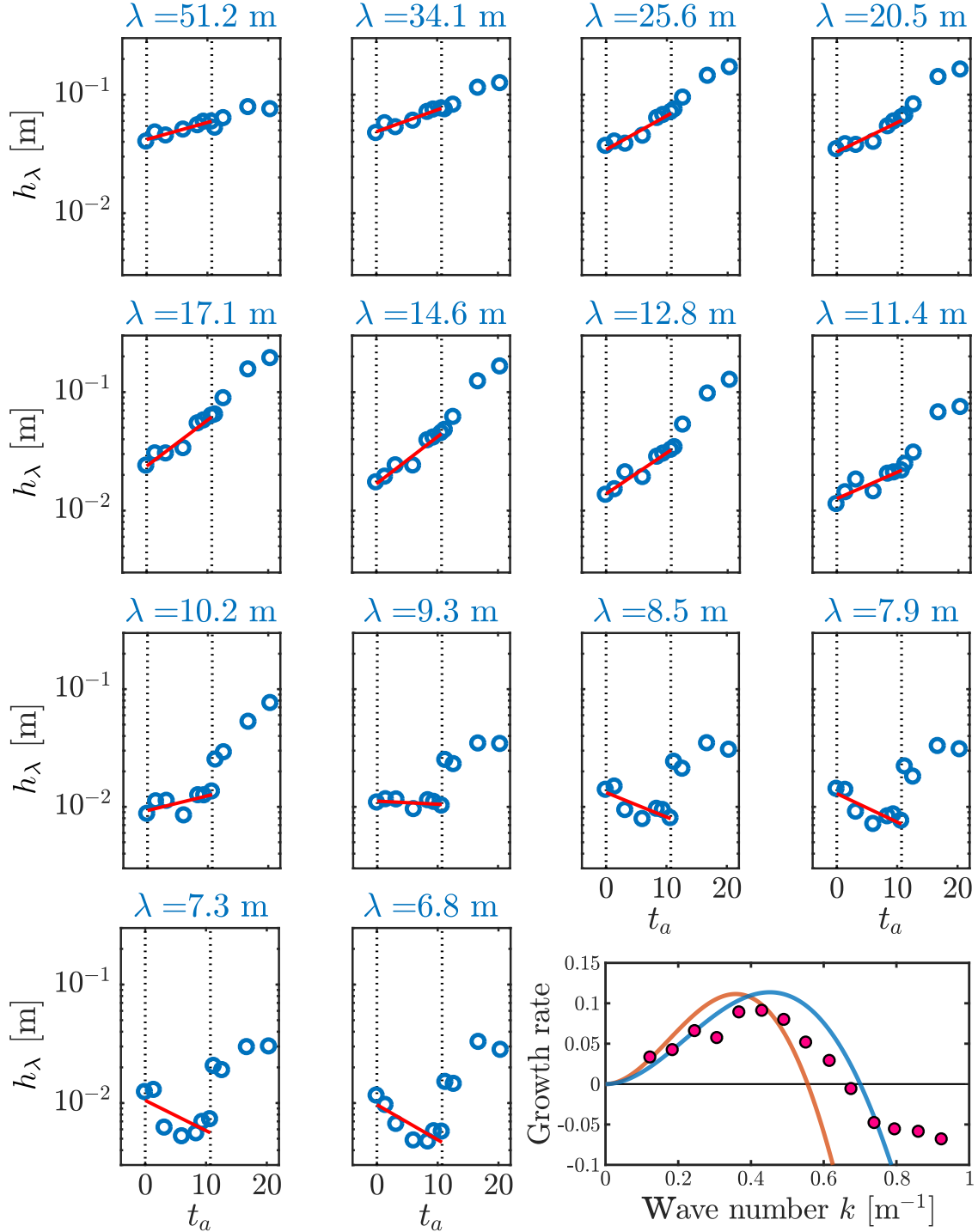


Figure S11: Growth rate of individual wavelengths. Considering the elevation profiles of transect N°20 and a sampling rate of 25 cm, figures show the logarithm of the amplitude h_λ of individual wavelengths with respect to the dimensionless time scale; $t_a = 0$ is set for April 10, 2014. Two different regimes are observed before and after $t_a = 10.7$, November 30, 2014. There are associated with the linear and non-linear growth phases. The growth rate of each wavelength is determined by an exponential fit performed during the linear phase ($0 \leq t_a \leq 10.7$, dashed lines). As a synthesis, the bottom right figure shows the dispersion relation, i.e. the growth rate with respect to the wave number $k = 2\pi/\lambda$. Solid lines are the same dispersion relations as in Fig. 6B of the main manuscript: $\{l_{\text{sat}}, A, B\} = \{0.95, 3, 1.5\}$ (orange) and $\{0.7, 1.96, 0.96\}$ (blue). Note that small wavelengths have amplitude of less than one centimeter. These amplitudes are comparable to the noise level of our topographic measurements, which prevents the estimation of the exponential decrease in growth rate for short wavelengths (≤ 8 m).

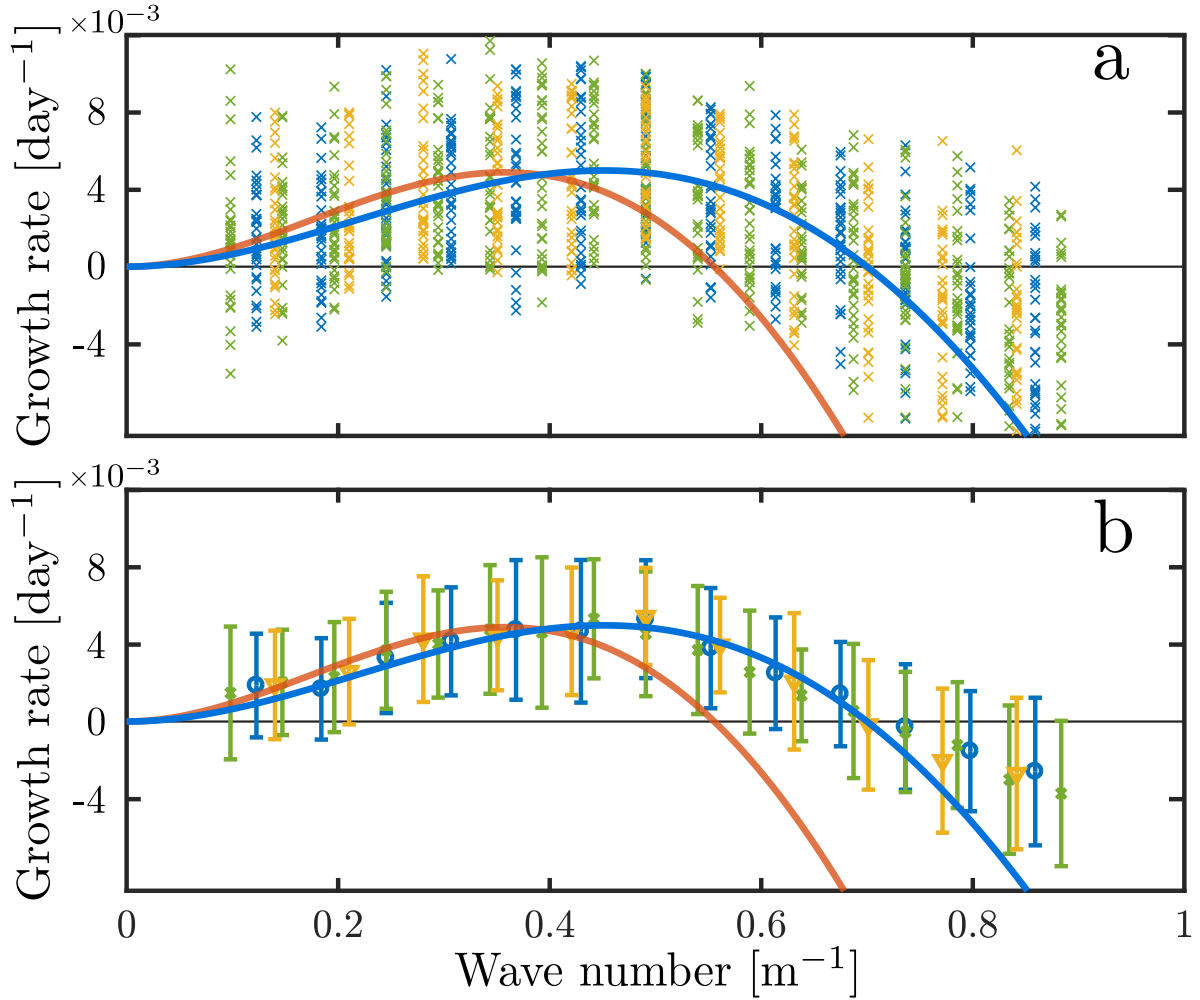


Figure S12: Dispersion diagram of the growth rate for all transects at different sampling rates. (a) Growth rates during the linear phase, i.e. from April 10, 2014 to November 30, 2014, with respect to the wave number $k = 2\pi/\lambda$ for each transect and sampling rates of 0.1 m (blue), 0.25 m (yellow) and 0.35 m (green). (b) Mean and standard deviation of the growth rates averaged on all transects. Solid lines are the same dispersion relations as in Fig. 6B of the main manuscript and in Fig. S11: $\{l_{\text{sat}}, A, B\} = \{0.95, 3, 1.5\}$ (orange) and $\{0.7, 1.96, 0.96\}$ (blue).

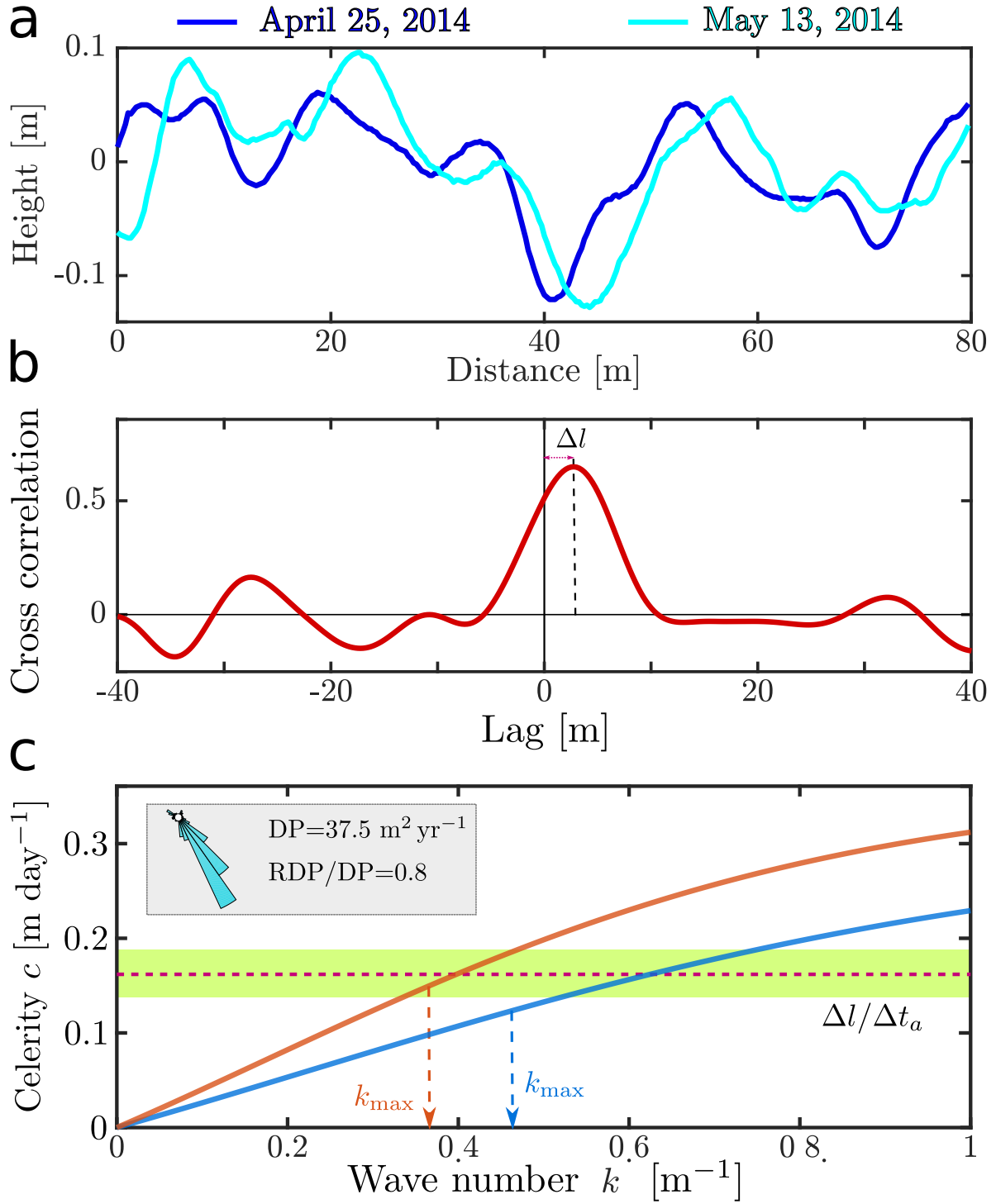


Figure S13: Dispersion diagram of the phase velocity. (a) Two consecutive elevation profiles of transect N° 16 during dune growth. (b) The maximum value of the cross correlation diagram between the two elevation profiles determines the dune migration distance $\Delta l = 3.25$ m from April 25 to May 13, 2014 (i.e. $\Delta t_a = 1.77$). (c) Dispersion diagram of the phase velocity using the same parameters as in Fig. 6B of the main manuscript and in Figs. S11 and S12b: $\{l_{\text{sat}}, A, B\} = \{0.95, 3, 1.5\}$ (orange) and $\{0.7, 1.96, 0.96\}$ (blue). Vertical dashed lines show the most unstable wavelength λ_{max} in both cases. Using cross correlation, the horizontal dashed lines shows the mean migration velocity $\Delta l / \Delta t_a$ averaged over all transects. The shaded area has a width of two standard deviation using the same data. There is a quantitative agreement between $c(\lambda_{\text{max}})$ and the migration rate derived from $\Delta l / \Delta t_a$. This is possible because during this period of time of the linear growth phase the wind regime is almost unidirectional (see inset).

- [3] Durán, O., Claudin, P. & Andreotti, B. On aeolian transport: Grain-scale interactions, dynamical mechanisms and scaling laws. *Aeolian Research* **3**, 243–270 (2011).
- [4] Fryberger, S. G. & Dean, G. Dune forms and wind regime. *A study of global sand seas* **1052**, 137–169 (1979).
- [5] Pearce, K. I. & Walker, I. J. Frequency and magnitude biases in the ‘Fryberger’ model, with implications for characterizing geomorphically effective winds. *Geomorphology* **68**, 39–55 (2005).
- [6] Tsoar, H. Sand dunes mobility and stability in relation to climate. *Physica A* **357**, 50–56 (2005).
- [7] Bagnold, R. The physics of wind blown sand and desert dunes: London (1941).
- [8] Sauermann, G., Kroy, K. & Herrmann, H. J. Continuum saltation model for sand dunes. *Physical Review E* **6403**, art. no.–031305 (2001).
- [9] Narteau, C., Zhang, D., Rozier, O. & Claudin, P. Setting the length and time scales of a cellular automaton dune model from the analysis of superimposed bed forms. *J. Geophys. Res.* **114** (2009).
- [10] Andreotti, B., Claudin, P. & Douady, S. Selection of dune shapes and velocities: Part 1: Dynamics of sand, wind and barchans. *Eur. Phys. J. B* **28**, 321–339 (2002).
- [11] Charru, F. Selection of the ripple length on a granular bed. *Phys. Fluids* **18**, 121–508 (2006).
- [12] Elbelrhiti, H., Claudin, P. & Andreotti, B. Field evidence for surface-wave-induced instability of sand dunes. *Nature* **437**, 720–723 (2005).
- [13] Fourrière, A., Claudin, P. & Andreotti, B. Bedforms in a turbulent stream: formation of ripples by primary linear instability and of dunes by nonlinear pattern coarsening. *Journal of Fluid Mechanics* **649**, 287–328 (2010).
- [14] Hersen, P., Douady, S. & Andreotti, B. Relevant length scale of barchan dunes. *Physical Review Letters* **89** (2002).
- [15] Andreotti, B. The song of dunes as a wave-particle mode locking. *Physical Review Letters* **93** (2004).
- [16] Andreotti, B., Claudin, P. & Pouliquen, O. Measurements of the aeolian sand transport saturation length. *Geomorphology* **123**, 343–348 (2010).
- [17] Pähtz, T., Kok, J. F., Parteli, E. J. & Herrmann, H. J. Flux saturation length of sediment transport. *Physical review letters* **111**, 218002 (2013).
- [18] Jackson, P. & Hunt, J. Turbulent wind flow over a low hill. *Q. J. R. Meteorol. Soc.* **101**, 929–955 (1975).

- [19] Sykes, R. I. An asymptotic theory of incompressible turbulent boundary layer flow over a small hump. *Journal of Fluid Mechanics* **101**, 647–670 (1980).
- [20] Claudin, P., Wiggs, G. & Andreotti, B. Field evidence for the upwind velocity shift at the crest of low dunes. *Boundary-layer meteorology* **148**, 195–206 (2013).